Journal of Non-Newtonian Fluid Mechanics 222 (2015) 190–208

Contents lists available at ScienceDirect

Journal of Non-Newtonian Fluid Mechanics

journal homepage: http://www.elsevier.com/locate/jnnfm

High-Weissenberg predictions for micellar fluids in contraction–expansion flows ☆

J.E. López-Aguilar [a], M.F. Webster [a,*], H.R. Tamaddon-Jahromi [a], O. Manero [b]

[a] Institute of Non-Newtonian Fluid Mechanics, College of Engineering, Swansea University, SA2 8PP, United Kingdom
[b] Instituto de Investigaciones en Materiales, UNAM, 04510, Mexico

ARTICLE INFO

Article history:
Received 2 June 2014
Received in revised form 25 November 2014
Accepted 28 November 2014
Available online 9 January 2015

Dedicated to Professor Ken Walters on the occasion of his 80th birthday.

Keywords:
High-elasticity solutions
Positive definiteness
Wormlike micelles
Bautista–Manero models
Hybrid finite element/volume method
Enhanced oil-recovery

ABSTRACT

This study is concerned with the numerical modelling of thixotropic and non-thixotropic materials in contraction–expansion flows at high Weissenberg number (*We*). Thixotropy is represented via a new micellar time-dependent constitutive model for worm-like micellar systems and contrasted against network-based time-independent PTT forms. The work focuses on steady-state solutions in axisymmetric rounded-corner 4:1:4 contraction–expansion flows for the benchmark solvent-fraction of $\beta = 1/9$ and moderate hardening characteristics ($\varepsilon = 0.25$). In practice, this work has relevance to industrial and healthcare applications, such as enhanced oil-reservoir recovery and microfluidics. Simulations have been performed via a hybrid finite element/finite volume algorithm, based around an incremental pressure-correction time-stepping structure. To obtain high-*We* solutions, both micellar and PTT constitutive equation *f*-functionals have been amended by (i) adopting their absolute values appealing to physical arguments (ABS-correction); (ii) through a change of stress variable, $\boldsymbol{\Pi} = \boldsymbol{\tau}_p + (\eta_{p0}/\lambda_1)\mathbf{I}$, that aims to prevent the loss of evolution in the underlying initial value problem; and finally, (iii) through an improved realisation of velocity gradient boundary conditions imposed at the centreline (VGR-correction). On the centreline, the eigenvalues of $\boldsymbol{\Pi}$ are identified with its $\boldsymbol{\Pi}$-stress-components, and discontinuities in $\boldsymbol{\Pi}$-components are located and associated with the *f*-functional-poles in simple uniaxial extension. Quality of solution is described through τ_{rz}, N_1 and N_2 (signature of vortex dynamics) stress fields, and $\boldsymbol{\Pi}$-eigenvalues. With {micellar, EPTT} fluids, the critical Weissenberg number is shifted from critical states of $We_{crit} = \{4.9, 220\}$ without correction, to $We_{crit} = \{O(10^2), O(10^3)\}$ with ABS–VGR-correction. Furthermore, such constitutive equation correction has been found to have general applicability.

© 2014 Elsevier B.V. All rights reserved.

1. Introduction

This study addresses the topic of high Weissenberg (*We*) number solutions for worm-like micellar systems using the class of Bautista–Manero models [1–4]. The work concentrates on the rounded 4:1:4 contraction/expansion benchmark flow problem, and various alternative procedural and constitutive approaches are introduced. Herein, high-elasticity levels are accessible through two routes: (i) a correction to the constitutive model based on physical arguments, in which absolute values of the dissipation–function components are considered in complex flow and (ii) the imposition of consistent boundary conditions at the axisymmetric geometry centre flow-line. There, in complex flow, the deformation is purely extensional (inhomogeneous) and shear-free flow prevails.

Worm-like micelle solution systems are a versatile family of fluids constituted by mixtures of surfactants – typically cetyltrimethylamonium bromide (CTAB) or cetylpyridinium chloride (CPyCl) – and salts – sodium salicylate (NaSal) in water [4,5]. These components interact physically, depending on the concentration, temperature and pressure, to form elongated micelles that entangle and provoke interactions of viscosity, elasticity, and breakdown and formation of internal structure [4]. This complex constitution spurns highly complex rheological phenomena, and manifests features associated with thixotropy [1], pseudo plasticity [1–4], shear banding [4] and yield stress [5]. These features render them as ideal candidates for varied processing and present-day applications, such as in use as drilling fluids in enhanced oil-reservoir recovery (EOR) [4], additives in house-hold-products, paints, cosmetics, health-care products, drag reducing agents [4,6].

Micellar constitutive models – Many approaches have been pursued to model wormlike micelle flow behaviour. The original Bautista–Manero–Puig (BMP) model [1,2,6] consisted of the

☆ Dedicated to Prof Ken Walters FRS on the occasion of his 80th Birthday.

* Corresponding author.
E-mail address: M.F.Webster@swansea.ac.uk (M.F. Webster).

http://dx.doi.org/10.1016/j.jnnfm.2014.11.008
0377-0257/© 2014 Elsevier B.V. All rights reserved.

upper-convected Maxwell constitutive equation to describe the stress evolution, coupled to a kinetic equation to account for structural flow-induced changes and, based on the rate of energy dissipation. Subsequently, Boek et al. [3] corrected the BMP model for its unbounded extensional viscosity in simple uniaxial extension – thus producing the base-form MBM model employed in the present analysis. This model has been tested in complex flow scenarios such as the benchmark 4:1 contraction flow [7] and 4:1:4 contraction–expansion flow [4], for which it has been proven inconsistent in excess pressure drop (EPD) predictions at the Stokesian limit. This anomaly has been dealt with recently [4] through a model that includes the viscoelasticity into the structure construction/destruction mechanism. Two variants for this model were considered with energy dissipation given by: (i) the polymer contribution exclusively (NM_τ_p model), and (ii) polymer and solvent contributions (NM_T model). These considerations introduce new physics into the representation, by coupling explicitly the thixotropic and elastic nature of these fluids, alongside new key rheological characteristics such as declining first normal stress difference in simple shear flow [4]. For completeness, one may cite other alternative model approaches that have appeared in the literature, though these have largely focused on simple flows and the shear-banding phenomena. The VCM model, based on a discrete version of the 'living polymer theory' of Cates, has been tested in simple flows, where rheological homogeneity prevails [8], and under conditions of shear-banding. Another approach consists of using the Johnson–Segalman model, modified with a diffusion term for the extra/polymeric stress (so-called d-JS model) [9]. The Giesekus model has also been used in the representation of wormlike micelles under simple shear scenarios, whilst using the non-linear anisotropy coupling parameter to introduce shear-banding conditions [10]. Another approach to shear-banded flows is that based on the two-fluid model [11]. Here, the interplay of flow-induced separations and rheology of the material studied has been analysed [11], which have been contrasted experimentally against pointwise flow-induced birefringence measurements [12].

One of the principal challenges in the field of computation rheology has been to address the problem of seeking convergent numerical solutions to the underlying partial differential equation system for steady-state complex flows at high levels of Weissenberg number, referred to as the so-called 'High-Weissenberg Number Problem' (HWNM) [13,14]. Strictly speaking this applies to the differential Maxwell/Oldroyd context, but in practice, often arises under strong-strain hardening alternatives, with shear-thinning (EPTT, LPTT, FENE-P; where *We*-definition may vary) or without shear-thinning (FENE-CR). Though many possible resolutions to this challenge have been proposed (see Walters and Webster [13], Keunings [14], Baaijens [15]), still for many complex flows there are often limitations in Weissenberg number solutions met – due to issues such as sharp stress boundary layers and flow singularities [16]. Relevant factors influencing the determination of a particular critical *We* solution state are: the numerical technique and discretisation for the independent variables (often stress, velocity, pressure, in space and time), the complex flow problem itself and the constitutive equation choice [14]. Here, and largely motivated by findings with thixotropic constitutive model adjustments, this issue is revisited and further light is cast upon the problem.

Variable transformation and positivity

Dupret et al. [17] and Dupret and Marchal [18] state that, for theoretical flows (i.e. simple flows, from which we extract material functions), a well-posed initial-value problem in the context of a Maxwell fluid is one in which: (a) the tensor $\boldsymbol{\Pi} = \boldsymbol{\tau}_p + (\eta_{p0}/\lambda_1)\boldsymbol{I}$) remains positive definite; (b) there are no solutions of a transient three-dimensional flow of a Maxwell fluid if the tensor $\boldsymbol{\Pi}$ does not remain positive-definite; (c) in a steady-state scenario with well-defined boundary conditions (i.e. with $\boldsymbol{\Pi}$ positive definite at the boundary that crosses the streamlines), a solution cannot exist when $\boldsymbol{\Pi}$ is non positive-definite; and (d) the change of mixed-type of the underlying differential equation system, from {elliptic to hyperbolic, steady} or {hyperbolic–parabolic to hyperbolic–hyperbolic, unsteady}, which influences the stability of the numerical scheme in terms of loss of evolutionary character, and by implication, the requirements (completeness – necessity and sufficiency) on boundary conditions themselves.

Application of positive definiteness principles to viscoelastic complex flows

Dupret et al. [17] applied the principles specified by Dupret and Marchal [18] to the finite element solution of Maxwell and Oldroyd-B fluids, dealing with 2D complex flows such as 4:1 contraction flow with sharp borders in planar and axisymmetric geometries, and flow past a cylinder. These authors found that Oldroyd-B solutions proved more stable in comparison with those with the Maxwell model, due to the solvent presence inherent in the former choice, which provides its contribution through solvent diffusion to the momentum transport. The stability of their numerical scheme was evaluated through an S-parameter, defined in terms of the eigenvalues of $\boldsymbol{\Pi}$ as $S = 2/(s_1/s_2 - s_2/s_1)$. This parameter characterises three possible outcomes: (i) $S > 0$, when both s_1, $s_2 > 0$; (ii) $S = 0$, when either s_1 or $s_2 = 0$ (not simultaneously); and (iii) $S < 0$, when s_1, s_2 have opposite signs. This last instance was denoted as a precursor and sign of numerical convergence problems (numerical breakdown in stable steady-state extraction, subject to an imposed and consistent detection criterion). Later, Dupret and Marchal [18] extended their studies on viscoelastic fluids for Johnson-Segalman and White Metzner equations, where '*evolutionary flows*' are those for which the '*solutions at a present time t is a valid initial condition for determining the flow fields at subsequent moments*', otherwise '*non-evolutionary flows*' are obtained. This classification was based on (a) the positive definiteness of the appropriate extra-stress tensor; and (b) the existence of an extremum in the determinant of the same tensor.

Classification of differential models and conformation-tensor form

Van der Zanden and Hulsen [19] and Hulsen [20] proposed a classification of differential models to analyse computationally inclusion of a Newtonian solvent contribution. In their work, they studied the Leonov and Giesekus models, finding that the inclusion of such a solvent contribution resulted in a more well-posed scheme for numerical computation (as argued above). With this in mind, Hulsen [21] generalised the work to define an alternative stress-like variable (as proposed similarly under Dupret and Marchal [18]), termed the configuration tensor, with its corresponding constitutive model statement, and with the objective of positive-definiteness retention under numerical solution. Here, the positive-definiteness of a differential constitutive equation system relies upon the property that the non-evolutionary terms therein remain positive and finite. Based upon such specification, corresponding expressions for equations of state were derived equivalent to commonly used models such as Giesekus and PTT.

The contraction–expansion flow problem offered in the current study is now a standard benchmark in experimental and computational rheology [13]. Some of the most outstanding features of this problem relate to its vortex dynamics (re-entrant/salient), stress fields, flow kinematics and pressure drop measurement [4]. Here, diverse manifestations of the nature of the fluid can be outlined, relating to vortex-size and evolution (extensional viscosity,

N_2-effects), structure formation and numerical tractability (sharp/rounded corners) [22,23]. One notes that the pressure drop, which reflects the energy expended in the flow, is often studied through an EPD measure [24,25], and itself offers a significant challenge to computational prediction [24].

2. Governing equations, constitutive modelling and theoretical framework

2.1. ABS and $\boldsymbol{\Pi}$ tensor approaches

Under transient, incompressible and isothermal flow conditions, the relevant mass conservation and momentum transport equations for viscoelastic flow, may be expressed in non-dimensional terms as (see definitions below; where here for conciseness the *notation on dimensionless variables is omitted)

$$\nabla \cdot \boldsymbol{u} = 0, \tag{1}$$

$$Re\ \frac{\partial \boldsymbol{u}}{\partial t} = \nabla \cdot \boldsymbol{T} - Re\ \boldsymbol{u} \cdot \nabla \boldsymbol{u} - \nabla p, \tag{2}$$

where t represents time; the gradient and divergence operators apply over the spatial domain; field variables $\boldsymbol{u}$, p and $\boldsymbol{T}$ represent fluid velocity, hydrodynamic pressure and stress contributions, respectively. Here, stress is split into a solvent part $\boldsymbol{\tau}_s$ (viscous-inelastic) and a polymeric contribution $\boldsymbol{\tau}_p$, $\boldsymbol{T} = \boldsymbol{\tau}_s + \boldsymbol{\tau}_p = 2\eta_s \boldsymbol{D} + \boldsymbol{\tau}_p$; $\boldsymbol{D} = (\nabla \boldsymbol{u} + \nabla \boldsymbol{u}^{\dagger})/2$ is the rate of deformation tensor, where the superscript † denotes tensor transpose. The dimensionless variables utilised are defined as follows:

$$\boldsymbol{x}^* = \frac{\boldsymbol{x}}{L}, \quad \boldsymbol{u}^* = \frac{\boldsymbol{u}}{U}, \quad t^* = \frac{U}{L}t, \quad \boldsymbol{D}^* = \frac{L}{U}\boldsymbol{D}, \quad \boldsymbol{\tau}_p^* = \frac{\boldsymbol{\tau}_p}{(\eta_{p0} + \eta_s)\frac{U}{L}},$$

$$p^* = \frac{p}{(\eta_{p0} + \eta_s)\frac{U}{L}}, \quad \boldsymbol{\Pi}^* = \frac{\boldsymbol{\Pi}}{\frac{\eta_{p0}}{\lambda_1}}$$

The non-dimensional group of the Reynolds number may be defined as $Re = \rho UL/(\eta_{p0} + \eta_s)$, with characteristic scales of U on fluid velocity (mean velocity, based on volume flow rate) and L on spatial dimension (based on minimum contraction-gap dimension). Material density is ρ and reference viscosity is taken as the zero shear-rate viscosity $(\eta_{p0} + \eta_s)$, so that $\frac{\eta_{p0}}{\eta_{p0}+\eta_s} + \frac{\eta_s}{\eta_{p0}+\eta_s} = 1.0$. Here, η_{p0} is the zero-rate polymeric-viscosity and η_s is the solvent-viscosity, from which the solvent fraction can be defined as $\beta = \eta_s/(\eta_{p0} + \eta_s)$.

A general statement of the differential constitutive model may be expressed in dimensionless form as:

$$We\ \overset{\nabla}{\boldsymbol{\tau}}_p = 2(1-\beta)\boldsymbol{D} - f_\tau \boldsymbol{\tau}_p, \tag{3}$$

where the upper-convected derivative of the extra-stress tensor is $\overset{\nabla}{\boldsymbol{\tau}}_p = \frac{\partial \boldsymbol{\tau}_p}{\partial t} + \boldsymbol{u} \cdot \nabla \boldsymbol{\tau}_p - \nabla \boldsymbol{u}^T \cdot \boldsymbol{\tau}_p - \boldsymbol{\tau}_p \cdot \nabla \boldsymbol{u}$. Here, a second dimensionless group number is introduced governing elasticity, via a Weissenberg number $(We = \lambda_1 U/L)$, which is a function of the characteristic material relaxation time, λ_1, and a characteristic rate – extracted from the characteristic velocity and length scales. Working within this general framework, and hence by specifying the functional f_τ, the networked nature of the fluid may be imposed, along with its theoretical properties.

With reference to the modelling of wormlike micellar systems, a new constitutive equation has recently been proposed [4] and adopted, with the *novel inclusion of viscoelasticity* within the destruction mechanics of the fluid network structure. Commencing from the Bautista–Manero–Puig (BMP) model [1,2], and its Modified Bautista–Manero (MBM) model counterpart [3], a non-linear dimensional differential structure equation for the fluidity $(\phi_p = \eta_p^{-1})$ emerges, from which the polymeric viscosity function η_p may be extracted. Then, the evolving space–time fluidity itself provides the distribution and dictates the construction–destruction dynamics of the fluid network-structure. Typically, this may begin from a fully structured-state to be converted to one of complete unstructured-state, using the energy dissipated by the polymer under flow. The present paper appeals to a version of this class of models, which combines the viscoelasticity into the thixotropic dependency, that of NM_τ_p, itself consisting of a stress-split form and polymeric contribution $\boldsymbol{\tau}_p$ as given by Eq. (3). Herein, dependency on fluidity $(\phi_p = \eta_p^{-1})$ arises through the dimensionless functional f_τ, which is given by the generalised differential structure equation, with $\boldsymbol{\zeta}$-variable used for stress [4]:

$$\frac{\partial f_\tau}{\partial t} = \frac{1}{\omega}(1 - f_\tau) + \xi_{G_0} We\ \boldsymbol{\zeta} : \boldsymbol{D}, \tag{4}$$

where the dimensionless functional f_τ is defined as $f_\tau = (\eta_{p0}/\eta_p)$, using η_{p0} as a viscous scaling factor on fluidity. Two versions of Eq. (4) arise and are reported elsewhere [4], dependent on the choice of $\boldsymbol{\zeta}$-variable: one, considering the energy dissipated by the polymer constituent to break the structure of the fluid ($\boldsymbol{\zeta} = \boldsymbol{\tau}_p$, NM_$\tau_p$ model); and the other, involving the polymer plus the solvent contributions ($\boldsymbol{\zeta} = \boldsymbol{T}$, NM_T model). The dimensionless parameters of this micellar model, which account for structural construction $(\omega = \lambda_s U/L)$ and destruction $[\xi_{G_0} = (k/\eta_\infty)G_0(\eta_{p0} + \eta_s)]$, appear in the corresponding terms for these mechanisms. When the dynamic differential Eq. (4) is recast into its steady-state form, then its equivalent algebraic form is recovered,

$$f_\tau = 1 + \omega \xi_{G_0} We\ \boldsymbol{\zeta} : \boldsymbol{D}. \tag{5}$$

Importantly, the dissipation function is the driving influence in model departure from Oldroyd behaviour ($f_\tau = 1$), which is modulated by the product of the construction and destruction parameters (thixotropy) with the Weissenberg number. Here, this expression for the f_τ-functional links directly with the viscosity, which is a positive physical quantity that should remain finite and above unity in scaled form ($\boldsymbol{\zeta} : \boldsymbol{D} \geqslant \boldsymbol{0}$),[1] during flow evolution (time) and throughout the spatial domain (in shear, extensional and mixed flow deformation). As such, negative values (and less than unity) of this f_τ-functional are inadmissible. As evidenced in our previous work [4], there are instances in complex 4:1:4 contraction/expansion flow, near numerical *We*-solution breakdown, in which the dissipation function becomes negative, thus predicting negative values of the f_τ-functional and unphysical thixotropic viscosities. To avoid this possibility arising, and consistent with the underlying ideal shear and extensional flow derivation theory, the following ABS-correction is proposed:

$$\frac{\partial f_\tau}{\partial t} = \frac{1}{\omega}(1 - f_\tau) + \xi_{G_0} We |\boldsymbol{\zeta} : \boldsymbol{D}|. \tag{6}$$

In Eq. (6), the absolute value sign is applied to each component of the scalar dissipation function.[2] This ABS-correction becomes redundant in simple shear and extensional flows, since the domain of the variables in such viscometric flows is positive. As such, this correction provides correct physical and thermodynamical interpretation to this family of micellar models, in their departure from ideal flow.

Under network theory, the well-known Phan–Thien Tanner models are considered which are frequently applied to represent the response of polymer melts (exponential, EPTT) and solutions (linear, LPTT), [26]. The constant, non-dimensional PTT parameter $\varepsilon \geqslant 0$ largely dictates severity in strain-hardening, with smaller values limiting to zero, offering the greater extremes in extensional viscosity (larger Trouton ratios). The same reasoning as with thixotropic models can be applied to PTT models, and the analysis returns towards classical Oldroyd-B behaviour in the limit of

[1] Note, observations on trace($\boldsymbol{\tau}_p$) > 0 of Hulsen [21], to maintain positive stored elastic energy with viscoelastic PTT models.

[2] Alternatively, apply the absolute operation to the total dissipative sum.

vanishing $tr\boldsymbol{\tau}_p$.[3] Consistently with the above f_τ-functional modifications expressed for thixotropic micellar models, the corresponding modification to the PTT models becomes:

$$f_\tau = 1 + \frac{\varepsilon}{1-\beta} We\ tr|\boldsymbol{\tau}_p| \text{ for LPTT, and}$$
$$f_\tau = \exp\left(\frac{\varepsilon}{1-\beta} We\ tr|\boldsymbol{\tau}_p|\right) \text{ for EPTT.} \quad (7)$$

Note, in Eq. (7), it is implied that the absolute value sign applies to every constituent component of the scalar $tr\boldsymbol{\tau}_p$. With PTT models, the trace of the extra-stress is the function responsible for departure from Oldroyd-B form, as opposed to dissipation, $\boldsymbol{\zeta}:\boldsymbol{D}$, under the thixotropic models.

Material functions for the models considered, along with the Oldroyd-B ($f = 1$) reference, are reported elsewhere [4]. The solvent fraction level considered in this work is the benchmark $\beta = 1/9$. The EPTT model ε parameters are chosen to take values at benchmark settings $\varepsilon = 0.25$ characterising polymer melts [4]. The resulting micellar extensional viscosity is matched with those of corresponding EPTT form at the $\{\varepsilon,\beta\}$ combination. The micellar construction and destruction parameters, matching EPTT extensional viscosity, are $\omega = 4.0$ and $\xi_{G0} = 0.1125$, respectively [4]. In this work, all the corrections targeted for modeling of micellar fluids have no effect on the viscometric material functions described in [4].

2.2. Change of variable (translations $\tau_p - \boldsymbol{\Pi}$)

Following the developments on positive definiteness and loss of evolution by Dupret and Marchal [18] and Hulsen [21], a *dimensional* tensor $\boldsymbol{\Pi} = \boldsymbol{\tau}_p + (\eta_{p0}/\lambda_1)\boldsymbol{I}$ is adopted in this study, which is a translation identity between $\boldsymbol{\Pi}$ and $\boldsymbol{\tau}_p$ tensors. As such, the eigenvalues of the $\boldsymbol{\Pi}$ tensor may be taken as a form of guidance as to solution quality and indeed, as an indicator towards violation in attaining converged steady-state numerical solutions at increasing *We*-increments (numerical divergence/breakdown). The *dimensionless* form of this tensor according to the non-dimensional variables above is $\boldsymbol{\Pi}^* = [We/(1-\beta)]\boldsymbol{\tau}_p^* + \boldsymbol{I}$.

Application of the $\boldsymbol{\Pi}$-tensor definition leads to the following *dimensionless* constitutive equation statement (omitting *notation):

$$We\ \overset{\nabla}{\boldsymbol{\Pi}} = -f_{\Pi}(\boldsymbol{\Pi} - \boldsymbol{I}). \quad (8)$$

For the time-dependent thixotropic micellar models, the functional f_{Π} is governed by the differential expression:

$$\frac{\partial f_{\Pi}}{\partial t} = \frac{1}{\omega}(1 - f_{\Pi}) + \xi_{G_0}(1-\beta)|\boldsymbol{\zeta}_{\Pi} : \boldsymbol{D}|, \quad (9)$$

which reduces under steady-state conditions to the following expression:

$$f_{\Pi} = 1 + \omega\xi_{G_0}(1-\beta)|\boldsymbol{\zeta}_{\Pi} : \boldsymbol{D}|. \quad (10)$$

For this family of fluids, it is noteworthy that the *We*-scaling on the non-dimensionalised dissipation function is omitted in the τ_p-to-$\boldsymbol{\Pi}$ translation. $\boldsymbol{\zeta}_{\Pi}$ represents the conformation-tensor form of $\boldsymbol{\zeta}$.

Then, the corresponding f_{Π}-functional for the time-independent network-based PTT models (see Hulsen [21]) are given by:

$$f_{\Pi} = 1 + \varepsilon tr|\boldsymbol{\Pi} - 3| \text{ for LPTT, and } f_{\Pi} = \exp(\varepsilon tr|\boldsymbol{\Pi} - 3|) \text{ for EPTT.} \quad (11)$$

One notes that Eqs. (9)–(11) already include the ABS-correction, yet this assumption may be relaxed to consider natural-signed options.

[3] Provided the model parameter set $\{\varepsilon, \beta, We\}>0$, as is necessary by definition.

2.3. $\boldsymbol{\Pi}$-eigenvalues in the field

The eigenvalues of any tensor can be calculated via the solution of the characteristic equation obtained as follows (applied to $\boldsymbol{\Pi}$)

$$\det(\boldsymbol{\Pi} - s\boldsymbol{I}) = 0, \quad (12)$$

where $\boldsymbol{s}$ denotes the vector of eigenvalues (s_i) of the tensor $\boldsymbol{\Pi}$. If we apply this principle to the symmetric $\boldsymbol{\Pi}$ tensor relevant to axisymmetric $\{z,r,\theta\}$-flow, as pertinent to this study with vanishing shear components – $\Pi_{r\theta} = \Pi_{z\theta} = 0$, given by:

$$\det\begin{pmatrix} \Pi_{zz} - s & \Pi_{rz} & 0 \\ \Pi_{rz} & \Pi_{rr} - s & 0 \\ 0 & 0 & \Pi_{\theta\theta} - s \end{pmatrix} = 0, \quad (13)$$

and thus producing the cubic characteristic equation:

$$[(\Pi_{zz} - s)(\Pi_{rr} - s) - \Pi_{rz}^2](\Pi_{\theta\theta} - s) = 0. \quad (14)$$

In this form, firstly note the decoupling of the $\theta\theta$-component from the remainder of the system, which provides the independence of the subsystem in r–z components (replicating that of planar flow). This is reflected in eigenvalue $s_3 = \Pi_{\theta\theta}$, which is termed the third eigenvalue and identified unambiguously with $\Pi_{\theta\theta}$ over the whole field. Then, the remaining two eigenvalues can be determined from the quadratic equation for the r–z subsystem:

$$(\Pi_{zz} - s)(\Pi_{rr} - s) - \Pi_{rz}^2 = 0, \quad (15)$$

which can be recasted as:

$$s^2 - (\Pi_{zz} + \Pi_{rr})s + (\Pi_{zz}\Pi_{rr} - \Pi_{rz}^2) = 0 \quad (16)$$

or more simply,

$$s^2 - tr\boldsymbol{\Pi}^{\text{sub}}s + \det\boldsymbol{\Pi}^{\text{sub}} = 0 \quad (17)$$

where use is made of trace and determinant operations, in $tr\Pi^{\text{sub}} = \Pi_{zz} + \Pi_{rr}$ and $\det\Pi^{\text{sub}} = \Pi_{zz} * \Pi_{rr} - \Pi_{rz}{}^2$.

Thus, the two solutions of Eq. (17) provide the first (s_1) and second (s_2) eigenvalues, respectively:

$$s_1 = \frac{tr\boldsymbol{\Pi}^{\text{sub}} + \sqrt{(tr\boldsymbol{\Pi}^{\text{sub}})^2 - 4\det\boldsymbol{\Pi}^{\text{sub}}}}{2}, \quad (18)$$

$$s_2 = \frac{tr\boldsymbol{\Pi}^{\text{sub}} - \sqrt{(tr\boldsymbol{\Pi}^{\text{sub}})^2 - 4\det\boldsymbol{\Pi}^{\text{sub}}}}{2} \quad (19)$$

Notably, the discriminant of the square-root represents a balance on sub-system components between the $(tr\ \boldsymbol{\Pi}^{\text{sub}})^2$ and $\det\boldsymbol{\Pi}^{\text{sub}}$, and to conform to real eigenvalues should comply with the restriction that $[(tr\ \boldsymbol{\Pi}^{\text{sub}})^2\text{-}4\det\boldsymbol{\Pi}^{\text{sub}}] \geqslant 0$.[4]

Corresponding and detailed analysis for the $\boldsymbol{\Pi}$-eigenvalues at the centreline (in shear-free flow) is given in Appendix A, along with their relationship to the poles of the f-functional in simple uniaxial extension. This detail is called upon in the results sections below.

2.4. Centreline shear-free boundary condition imposition – VGR-correction

Consistent boundary conditions are required for any differential problem to be well-posed. In the contraction–expansion flow problem, the symmetry flow-line is the unique region in the flow-domain where uniaxial (inhomogeneous) extension exclusively occurs, as opposed to the contraction-wall where (inhomogeneous) shear flow prevails. Conventionally, the so-called stick-boundary

[4] In practice, this condition has always been met for computable and stable steady-state *We*-solutions.

condition is assumed along the contraction-wall, by which the fluid is treated as at rest on the wall ($\boldsymbol{u} = 0$). At the shear-free centreline, flow symmetry boundary conditions apply. In this work, under VGR-correction and on the centreline, we propose imposing specific analytical restrictions on the deformation gradients (see section below). Here, the deformation gradients themselves are determined throughout the flow domain by a superconvergent local recovery technique and imposed on the stress equation (akin to well-known DEVSS-G methodology, but applied locally in quadratic form [27]). This enforces: (i) shear-free flow, to ensure 1D-extensional deformation (Eq. (20a)); (ii) a pure uniaxial extension relationship between the normal deformation-gradients (Eq. (20b)); and (iii) nodal-pointwise continuity imposed exactly, in discrete form (Eq. (20c)). With computed knowledge of the normal deformation-gradients, the third of these conditions may be utilised throughout the domain, irrespective of 1D-centreline arguments. Assuming specific notation for the extensional rate on the centreline in the axial direction, as $\hat{\dot{\varepsilon}} = \frac{\partial u_z}{\partial z}$,[5] then the following identities may be established and imposed on the numerical solution under VGR-correction:

$$\frac{\partial u_z}{\partial r} = \frac{\partial u_r}{\partial z} = 0, \tag{20a}$$

$$\frac{\partial u_r}{\partial r} = -\frac{1}{2}\frac{\partial u_z}{\partial z} = -\frac{1}{2}\hat{\dot{\varepsilon}}, \tag{20b}$$

$$\frac{u_r}{r} = -\left(\frac{\partial u_z}{\partial z} + \frac{\partial u_r}{\partial r}\right) = -\frac{1}{2}\hat{\dot{\varepsilon}}. \tag{20c}$$

Corresponding solutions results are discussed below, when this methodology is considered. As such, the VGR-correction is intended to eliminate noise proliferation, originating at the centreline, which may provoke numerically polluted solutions and earlier numerical solution breakdown.

3. Problem specification and numerical schemes

The schematic representation of the 4:1:4 axisymmetric, rounded-corner contraction/expansion flow problem with its corresponding mesh data are reported elsewhere [4,25]. See Aguayo et al. [25] for further detail on this problem, which provides a full mesh refinement analysis for some typical case studies.

3.1. Hybrid finite element/finite volume scheme

The hybrid finite element/volume scheme is a semi-implicit, time-splitting, fractional three-staged formulation, which draws upon finite element discretisation for velocity–pressure approximation and finite volume for stress [27–29]. In brief, Galerkin *fe*-discretisation is applied to the embedded Navier–Stokes system components; the momentum equation at stage-1, the pressure-correction equation at stage-2 and the incompressibility satisfaction constraint at stage-3 (to ensure higher order precision). The *fv*-tessellation is constructed from the *fe*-grid by connecting the mid-side nodes. Stress variables are located at the vertices of *fv*-sub-cells (cell-vertex method, equivalent to linear interpolation). In contrast, quadratic velocity interpolation is enforced on the parent *fe*-cell, alongside linear pressure interpolation. A direct solution method is employed at the *fe* pressure-correction stage-2, whilst a space-efficient element-by-element Jacobi iteration is preferred over the remaining stages one and three, under the *fe*-components.

3.2. Stress-finite volume cell vertex scheme

Cell-vertex *fv*-scheme applied to extra-stress are based upon an upwinding technique (fluctuation distribution), which distributes control volume residuals to provide nodal solution updates. Concisely, by rewriting the extra-stress equation in non-conservative form, with flux ($\boldsymbol{R} = \mathbf{u}\cdot\nabla\boldsymbol{\tau}$) and absorbing remaining terms under the source (Q), one may obtain:

$$\frac{\partial \boldsymbol{\tau}}{\partial t} + \boldsymbol{R} = \boldsymbol{Q}. \tag{21}$$

We consider each scalar stress component, τ, acting on an arbitrary volume $\Omega = \sum_l \Omega_l$, whose variation is controlled through corresponding components of fluctuation of the flux vector (R) and the source term (Q),

$$\frac{\partial}{\partial t}\int_{\Omega_l} \tau d\Omega = \int_{\Omega_l} R d\Omega + \int_{\Omega_l} Q d\Omega. \tag{22}$$

The objective is to evaluate the flux and source variations over each finite volume triangle (Ω_l), with their distribution to its three vertices according to the preferred strategy. The resulting nodal update for a particular node (l) is obtained by accumulating the contributions from its control volume Ω_l, composed of all *fv*-triangles surrounding node (l). The flux and source residuals may be evaluated over different control volumes associated with a given node (l) within the *fv*-cell T; namely, the contribution governed over the *fv*-triangle T, (R_T, Q_T), and that subtended over the median-dual-cell zone, (R_{mdc}, Q_{mdc}) [30]. This procedure demands appropriate area-weighting to maintain consistency, which for temporal accuracy has been extended to time-terms likewise. With the candidate stress equation considered as split into time derivative, flux and source, and integrated over associated control volumes, the concise generalized *fv*-nodal update equation may be expressed per stress component as,

$$\left[\sum_{\forall T_l}\delta_T \alpha_l^T \Omega_T + \sum_{\forall MDC_l}(1-\delta_T)\widehat{\Omega}_l^T\right]\frac{\Delta\tau_l^{n+1}}{\Delta t} = \sum_{\forall T_l}\delta_T\alpha_l^T b^T + \sum_{\forall MDC_l}(1-\delta_T)b_l^{MDC}, \tag{23}$$

where $b^T = (-R_T + Q_T)$, $b_l^{MDC} = (-R_{MDC} + Q_{MDC})^l$. Here, Ω_T is the area of the *fv*-triangle T, whilst $\widehat{\Omega}_l^T$ is that of its median-dual-cell (MDC). Parameter δ_T directs the balance taken between the contributions from the median-dual-cell and the *fv*-triangle T, with $0 \leqslant \delta_T \leqslant 1$ [29]. This expression recognizes segregated fluctuation distribution and median dual cell contributions, area weighting and upwinding factors (α_l^T-scheme dependent).

3.3. Velocity-gradient approximation (VGR-correction)

In Webster and co-workers [27,31], both local (direct-recovery) and global (Galerkin) schemes for the treatment of velocity-gradients (VGR) were analysed and compared. There, a direct and nodal method was advocated, based on averaging velocity-gradient elemental-contributions to a triangular mesh-node. It is particularly significant that for midside nodes, this is the only scheme that enjoys superconvergent properties. In contrast, the global Galerkin approach fits an appropriate set of nodal gradient values that satisfy an associated weighted-residual formulation. Hawken et al. [31] observed that the local recovery method offered improved performance, for solution gradients in complex flow problems, such as flow past a cylinder. Likewise, Matallah et al. [27] conducted similar analysis on a 4:1 contraction problem and flow around a cylinder, observing that the local recovery technique was more stable than a local Galerkin equivalent; see summary in Walters and Webster [13]. Furthermore, in Belblidia et al. [28] the above analysis was revisited under velocity-stress, parent/subcell approximation, as used here. This covered the various function-spaces and combination-options available for velocity-gradient representation (parent/subcell control-volume, quadratic/linear order), with special reference to stress-subcell

[5] As a function of z-spatial variable, in uniaxial extension along the flow centreline.

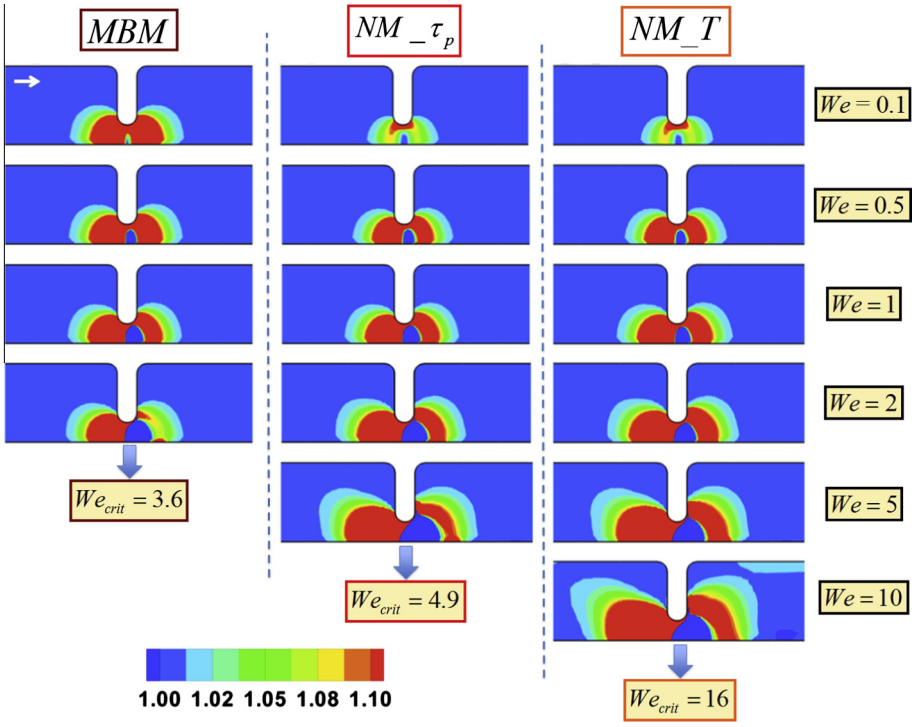

Fig. 1. f_τ-functional 2D-fields versus *We*; MBM, NM_τ_p and NM_T.

approximation. In [28], the localised-quadratic velocity-gradient (parent-cell) treatment was shown to achieve both stability and accuracy, applying robustly for both linear (subcell) and quadratic (parent) stress interpolations.

Entry flow kinematics are determined computationally for the equivalent entry-channel problem. These may be imposed through the time-stepping procedure, either as steady-state, or via a smooth transient build-up. Then, fully-developed outflow conditions are established ensuring no change in streamwise and vanishing cross-stream kinematics. Once fully-developed entry-flow kinematic are known, stress may be determined through the derived and corresponding initial-value-problem ODE system (consistent with internal domain solution discretisation).

4. Solutions with Micellar NM_τ_p model – natural-signed form

4.1. Negative *f*-values in complex flow

In Fig. 1, zones of small and negative f_τ-value, appear at the centreline from low *We*-solution levels onwards (i.e. *We* = 0.1, dark blue[6] regions). These regions grow towards the contraction wall and are convected downstream as elasticity level increases, for all three micellar models (i.e. MBM, NM_τ_p, NM_T) [4], which vary in dissipation function. Regarding the colour-scale, the darkest blue in the scale represents the value of unity for the f_τ-functional. Consistently, as $f_\tau = 1$ is the smallest value in the colour-scale, values of $f_\tau < 1$ are represented with the darkest blue regions. This style of colour-scale has been adopted to precisely detect/highlight the presence and size of regions with $f_\tau < 1$.

The structure equation given in terms of the *f*-functional for the micellar models is represented in $[1 + g(\zeta{:}\boldsymbol{D})]$ form. The only way this expression can generate negative *f*-values in complex flow is if $g(\zeta{:}\boldsymbol{D}) \leftarrow 1$. This occurrence is unphysical with respect to the second law of thermodynamics, since any viscous flow is dissipative; thus increasing the entropy of the system [32]. Moreover, the *f*-functional for these thixotropic micellar models is explicitly related to viscosity-inverse (see Eq. (4)). Thus, negative *f*-values represent negative viscosities in the field (again unphysical); and moreover, when $g(\zeta{:}\boldsymbol{D}) = -1$, $f = 0$, an infinite viscosity would be predicted. As reported elsewhere [4], numerical breakdown for each micellar variant, characterised by the critical-*We* (denoted We_{crit}) solution, is observed when the small and negative *f*-function region reaches the contraction wall (see Fig. 1 and Table 1). In this study, for the sake of conciseness only, the NM_τ_p micellar version is studied in detail; nevertheless, all observations are quite general.

4.2. s_2-field trends and numerical breakdown

In Fig. 2, the evolution of NM_τ_p s_2-fields through increasing elasticity to We_{crit} is depicted. This graduated change in solution state with elasticity level is evidence to the regional loss of positive-definiteness and the consequence this has on evolution in *We*-solution, which provokes numerical breakdown [18]. Firstly, at low elasticity levels (*We* = 0.5) (Fig. 2a), s_2 remains positive throughout the field, with variations about the centreline given by the mixed nature of shear–extensional flow. The s_2-minimum value ($s_{2\min} = 0.53$; see Table 2) is located on the centreline, downstream with respect to the contraction. This first low s_2 peak (blue spot on centreline; see 2D field) is connected to the contraction wall by another light-blue positive contour level, originating at the centreline and reaching out across the flow to the contraction wall. The s_2-maximum value (red spot $s_{2\max} = 1.03$) is located off the centreline, but close to it; this is surrounded by a green contour-banded region of relatively low-s_2 levels, that connects locations on the centreline to those on the wall, both upstream and downstream of the contraction.

Interestingly, when elasticity level is increased further to *We* = 2 (Fig. 2b), negative-blue s_2 values begin to penetrate into the field. The location of the minimum-negative value is observed through the first-peak at the centreline ($s_{2\min} = -0.23$), which appears to

[6] For interpretation of colour in Figs. 1, 2, 6, 8, B1 and B2, the reader is referred to the web version of this article.

Table 1
f_τ, f_{Π} extrema versus *We*; micellar models.

We		f_τ			f_{Π}
		Natural	ABS	VGR	$\boldsymbol{\Pi}$
0.1	Max.	2.06	2.06	2.06	2.69
	Min.	0.998	1.00	1.00	1.00
0.5	Max.	4.11	4.18	4.18	5.82
	Min.	0.87	1.00	1.00	1.00
1	Max.	5.62	6.59	6.59	7.87
	Min.	0.59	1.00	1.00	1.00
2	Max.	7.4	10.94	10.94	12.14
	Min.	−0.34	1.00	1.00	1.00
3	Max.	8.72	13.35	13.35	15.07
	Min.	−1.82	1.00	1.00	1.00
4	Max.	9.98	15.39	15.39	17.58
	Min.	−3.44	1.00	1.00	1.00
5	Max.	11.04[a]	17.35	17.35	19.92
	Min.	−4.91	1.00	1.00	1.00
10	Max.		25.48	25.48	30.40
	Min.		1.00	1.00	1.00
15	Max.		32.20	32.20	41.72
	Min.		1.00	1.00	1.00
20	Max.		36.85	36.85	42.65
	Min.		1.00	1.00	1.00
30	Max.		41.29	41.29	53.19
	Min.		1.00	1.00	1.00
40	Max.		74.51[b]	85.54	115.87
	Min.		1.00	1.00	1.00
75	Max.			195.49	256.53
	Min.			1.00	1.00
100	Max.			279.89	321.52
	Min.			1.00	1.00
140	Max.			427.52	450.44
	Min.			1.00	1.00
175	Max.			534.31	562.73
	Min.			1.00	1.00
200	Max.			606.83	
	Min.			1.00	
250	Max.			748.47	
	Min.			1.00	
370	Max.			1037.10	
	Min.			1.00	

[a] $We_{crit} = 4.9$.
[b] $We_{crit} = 39$.

be convected downstream. This negative region remains connected to that on the contraction wall by a similar green-positive fringe to that identified when *We* = 0.5. In addition, this green fringe (disconnected downstream) partially surrounds the second-red positive-peak. This second-red peak appears to have grown in size and strength ($s_{2max} = 1.24$), and is convected downstream in contrast to the *We* = 0.5 solution. Moreover, a new feature has now arisen at this *We*-level: a third peak on the downstream contraction wall (see 3D field-plot). The value for this peak ($s_2 = 0.27$ units) remains positive. The fully-developed flow region upstream and downstream of the contraction is characterised by levels of $0.8 \leqslant s_2 \leqslant 1$ units.

Fig. 2c provides corresponding results at *We* = 3. Here, strong features in s_2 are established which become more intense with rise in *We*. The first and second-peaks, are identified by $s_{2min} = -0.29$ and $s_{2max} = 1.35$, respectively; these have been convected even more and become relatively more intense, with reference to lower *We*-level solutions. At *We* = 3, the positive surrounding-level connecting the first-peak between the centreline and contraction wall, appears larger and fully-connected upstream. The third-peak at the downstream wall has become sharper and its local minimum value has just wandered into negativity ($s_2 = -0.05$).

Finally and most conspicuously for *We* = 4.9, the stage is reached beyond which steady-state numerical breakdown is observed (Fig. 2d, $We_{crit} = 4.9$, breakdown at *We* = 5). Note, the important switch in location of the global $s_{2min} = -2.05$ in the NM_τ_p case at $We_{crit} = 4.9$, from previous *We*-levels on centreline, to presently on the wall (backface-tip of contraction). In addition here, a fourth-red positive-peak also becomes apparent on the downstream wall, next to the third-peak, as fresh evidence to the appearance of solution overshoot–undershoot. Moreover, the first two peaks appear completely attached to the centreline and convected downstream. The first-peak has become less intense at this *We*-level ($s_2 = -0.15$), whilst the second-peak has grown in size and intensity ($s_{2max} = 1.39$). The first-peak at the centreline still remains connected to the wall by a slim-positive s_2-band (light-blue).

4.3. s_1–s_2 versus $\boldsymbol{\Pi}_{zz}$-$\boldsymbol{\Pi}_{rr}$ @ centreline

In Fig. 3, a plot for NM_τ_p data at $We_{crit} = 4.9$ illustrates the theory of Section 2.4 for the swapping-over character of the eigenvalues at centreline. As predicted by the theory, $s_1 = \boldsymbol{\Pi}_{zz}$ and $s_2 = \boldsymbol{\Pi}_{rr}$ when N_1 remains positive, whilst $s_1 = \boldsymbol{\Pi}_{rr}$ and $s_2 = \boldsymbol{\Pi}_{zz}$ when N_1 becomes negative. The switch-over point in N_1 lies at $z = 1.6$ units (at $We_{crit} = 4.9$). Interestingly, the switch-over point in N_1-sign is independent of counterpart conditions in rate of deformation. Along this flow-line, uniaxial extension is apparent upstream and uniaxial compression downstream. Moreover, given that a constant flow rate is maintained in these λ_1-increasing simulations, the localised inhomogeneous rate of deformation is barely changed throughout the *We*-continuation procedure.

4.4. $\boldsymbol{\Pi}_{zz}$–$\boldsymbol{\Pi}_{rr}$ versus f_{Π}-functional poles @ centreline

As discussed in Appendix A and applicable on the centreline, a correlation may be extracted between numerical $\boldsymbol{\Pi}$-components and their corresponding simple uniaxial extensional predictions from viscometric/linear viscoelastic regime theory. Fig. 4 gathers this comparison together at low elasticity levels *We* = {0.001, 0.01, 0.1}. As *We* tends to zero, the continuous reference line is that of unity. As elasticity is elevated, the inhomogeneous nonlinear solution is contrasted against its linearised inhomogeneous counterpart. To be precise, the latter is extracted functionally from viscometric theory along the centreline, yet by imposing the derived inhomogeneous state of stress and deformation from the numerical solution. The numerical data curves at *We* = 0.001, for $\boldsymbol{\Pi}_{zz}$ (symbols) and its theoretical linear estimation (f-pole$_1$ related to $2\dot{\varepsilon}We$ – dashed lines) are practically superimposed over the reference line. For *We* = 0.01, departure from viscometric data is now evident, yet not relatively significant, ranging around 2% for the largest departure. In contrast for *We* = 0.1, this departure appears significantly large, with the largest difference ranging around 25% over the unity reference line. Comparison of $\boldsymbol{\Pi}_{rr}$ with its theoretical linear estimation (f_{Π}-functional-pole$_2$ related to $\dot{\varepsilon}We$ – dashed lines; see inset Fig. 4) provides similar trends as pole$_1$ analysis, with two main differences: (i) at *We* = 0.1, the maximum departure of the linear estimation from unity reference line, is smaller (14%) than occurs with f_{Π}-functional-pole$_1$, and (ii) now, the maximum departure appears downstream. Note, the shape of $\boldsymbol{\Pi}_{rr}$ is the reflected-scaled image of $\boldsymbol{\Pi}_{zz}$ in the reference line; also, all curves intersect at $z = 0$.

Fig. 5 provides additional information at more elevated elasticity levels, including $We_{crit} = 4.9$. At *We* = 0.5, a singularity in $\boldsymbol{\Pi}_{zz}$ linear viscometric estimation is observed at $z \sim -0.9$. The reason for their appearance is illustrated in the plot below, in which a

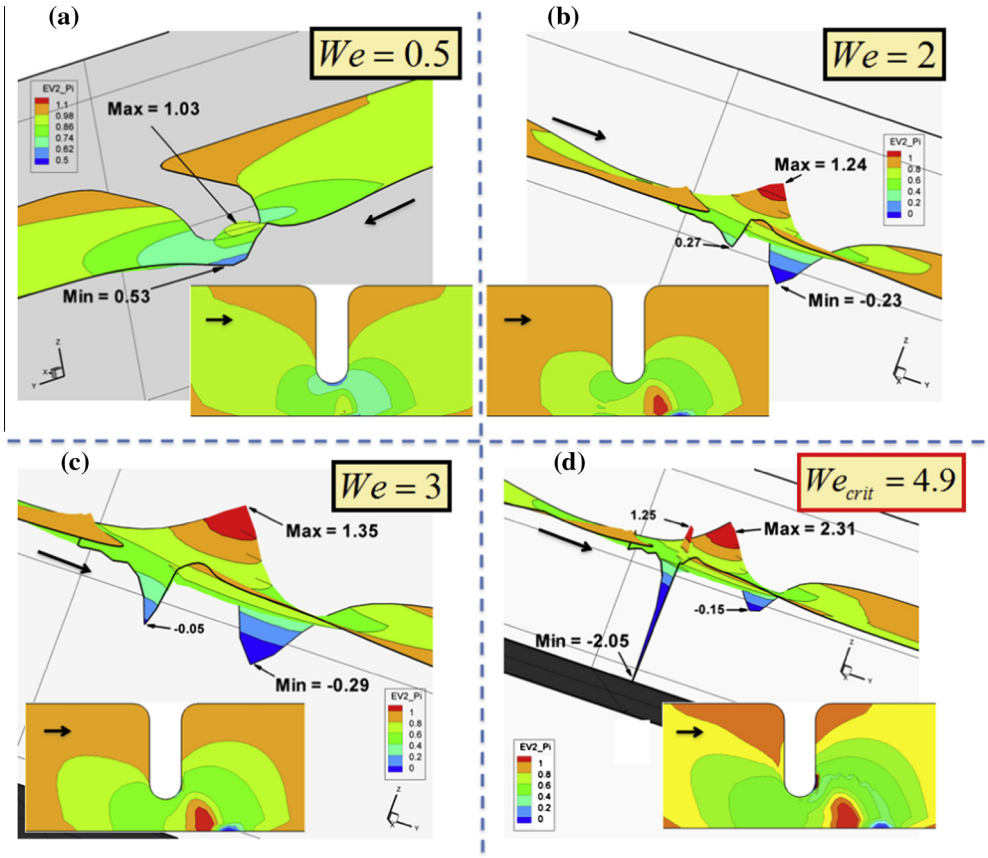

Fig. 2. s_2 2D, 3D-fields versus *We*; NM_τ_p.

comparison between the $\boldsymbol{\Pi}_{zz}$ viscometric estimation (top-row) and the components of the pole$_1$ (bottom-row) are plotted as *We* rises and complex flow becomes more dominant. These singularities correspond in location to the centreline-zone at which the components of pole$_1$ (i.e. $f_{\boldsymbol{\Pi}}$ and $2\dot{\varepsilon}We$) balance one another (bottom-row). A similar situation arises with $f_{\boldsymbol{\Pi}}$-functional-pole$_2$ (i.e. $f_{\boldsymbol{\Pi}}$ and $-\dot{\varepsilon}We$), for which singularities are observed first at larger $We = 2$ relative to $f_{\boldsymbol{\Pi}}$-functional-pole$_1$.

5. The ABS correction – Micellar NM_τ_p_ABS model and larger We_{crit}

5.1. Correction on negative f-values and consequence on positive definiteness

To correct for the inconsistency in the f_τ-functional, and therefore in viscosity predictions described in Section 4, these thixotropic models have been amended – adopting absolute components values in the dissipation function (see Section 2.1). Considering such ABS-correction provides the global $f_{\tau_min} = 1$ (extrema, Table 1), applicable spatially and through all *We*-levels for NM_τ_p_ABS. In contrast, NM_τ_p provides negative values ($f_{\tau_\min} = -4.92$) at $We_{\text{crit}} = 4.9$. Moreover, global f_{τ_max} is observed to increase. For example, this extremum for $We = \{2,3,4,4.9\}$ goes from $f_{\tau_\max} = \{7.40, 8.72, 9.98, 11.04\}$ for NM_τ_p, to $f_{\tau_\max} = \{10.94, 13.35, 15.39, 17.34\}$ with $We = \{2,3,4,5\}$ and NM_τ_p_ABS. Fig. 6 compares f_τ and s_2 in 2D and 3D-fields at $We = 4.9$ (We_{crit} for NM_τ_p). Consistently, the blue-region containing negative NM_τ_p f_τ-functional values is lost in NM_τ_p_ABS 2D-fields, and replaced by a continuous red-region about the contraction. The 3D-f_τ-fields reveal further detailed features, with NM_τ_p providing (i) a pronounced negative-dip just downstream of the contraction and filling the gap across the flow; and (ii) a sharp negative-peak to this f_τ-dip at the downstream contraction-wall ($f_\tau = -3.37$); which now coincides in location with the negative-peak observed in the second eigenvalue data ($s_{2\min} = -2.05$). In contrast, NM_τ_p_ABS 3D-f_τ-field data provides a less-erratic field about the contraction, with two local maxima $f_\tau = \{4.51, 3.86\}$, and a minimum $f_\tau = 1.35$ at the centreline. Note under NM_τ_p_ABS, values of f_τ slightly larger than unity are located over the *fully-developed regions*, upstream and downstream of the contraction, where shear flow prevails. $f_\tau$values grow with increasing *We* and along the radial direction at any fixed *z*-coordinate in these locations; from $f_{\tau min} = 1$ at the centreline (since $\tau_{rz} = 0$, hence $\boldsymbol{\tau}_p : \boldsymbol{D} = \tau_{rz}\left(\frac{\partial u_z}{\partial r} + \frac{\partial u_r}{\partial z}\right) = 0$), to f_τ values larger than unity at the wall (where $\boldsymbol{\tau}_p : \boldsymbol{D} \neq 0$). For instance, the NM_$\tau_p$_ABS solution at $We_{\text{crit}} = 39$, provides f_τ-values that range between $f_{\tau\min} = 1$ at the centreline, and $f_\tau = 1.06$ at the wall.

5.2. 2D and 3D field s_2 and N_1-data

Furthermore, the s_2-data counterpart to f_τ-data in Fig. 6 (see more in Fig. B1), clearly exhibits the strong influence of the ABS-correction: the sharp negative-peak on the wall observed in NM_τ_p results is practically lost under NM_τ_p_ABS. With NM_τ_p_ABS, this key contraction-wall feature appears positive ($s_2 = 0.24$) and relatively less prominent; whilst it is negative ($s_{2\min} = -2.05$; Table 2) and sharp in the natural-signed NM_τ_p results. Moreover, overshoot–undershoot in s_2 is absent at this location for NM_τ_p_ABS, whilst this is evident in the NM_τ_p 3D-field data, through a prominent positive red-peak ($s_2 = 1.25$) next to the negative blue-peak ($s_{2\min} = -2.05$). One notes, the severity of solution gradients at this location and degradation in the quality of their capture, which all

Table 2
s_2 extrema versus *We*; micellar models.

We		s_2			
		Natural	ABS	VGR	Π
0.1	Max.	1.00	1.00	1.00	1.00
	Min.	0.74	0.74	0.74	0.74
0.5	Max.	1.03	1.03	1.03	1.01
	Min.	0.53	0.55	0.55	0.48
1	Max.	1.13	1.09	1.09	1.06
	Min.	0.10	0.17	0.17	0.24
2	Max.	1.24	1.22	1.22	1.22
	Min.	−0.23	−0.11	−0.11	0.03
3	Max.	1.35	1.31	1.31	1.31
	Min.	−0.29	−0.18	−0.18	−0.04
4	Max.	1.52	1.4	1.4	1.41
	Min.	−0.80	−0.19	−0.2	−0.05
5	Max.	2.31[a]	1.47	1.47	1.49
	Min.	−2.05	−0.22	−0.22	−0.08
10	Max.		1.75	1.74	1.83
	Min.		−0.28	−0.3	−0.13
15	Max.		1.98	1.97	2.11
	Min.		−0.96	−0.96	−0.69
20	Max.		2.17	2.17	2.3
	Min.		−2.00	−2.00	−95.75
30	Max.		2.57	2.57	2.91
	Min.		−109.98	−109.97	−105.67
40	Max.		2.82[b]	2.75	3.15
	Min.		−143.55	−154.13	−258.04
75	Max.			7.82	3.89
	Min.			−354.61	−490.08
100	Max.			10.73	3.88
	Min.			−474.41	−665.58
140	Max.			6.77	5.04
	Min.			−663.73	−932.55
175	Max.			9.33	6.05
	Min.			−791.01	−1166.40
200	Max.			10.34	
	Min.			−902.81	
250	Max.			11.81	
	Min.			−1124.60	
370	Max.			17.30	
	Min.			−1641.20	

[a] $We_{crit} = 4.9$.
[b] $We_{crit} = 39$.

hints at pending numerical solution breakdown. The global s_{2min} is smaller and on centreline (*cl*) for NM_τ_p_ABS compared with NM_τ_p, noting the final $We = 4.9$ s_{2min} value switches location from -0.19_{cl} to -2.05_{wall}. At fixed $We = 4.9$, contrasting *local* s_{2min} *on centreline* between NM_τ_p_ABS and NM_τ_p solutions and (Fig. 6), reveals an even more intense peak for NM_τ_p_ABS (global $s_{2min} = -0.19$) relative to NM_τ_p (*local* $s_{2min} = -0.15$). See Appendix B for additional data on stress fields. Corresponding N_1-field data reveal analogue features compared to s_2-fields. Particularly the location of the local extrema values in both natural-signed and ABS fields. For NM_τ_p, $s_{2min} = -2.05$ and $N_{1min} = -3.53$ lie on the back-face wall of the contraction, in the form of a sharp peaks. In contrast, NM_τ_p_ABS display s_2-positive values and a relatively reduced global $N_{1min} = -1.93$ at the back-face wall of the contraction. At the centreline, NM_τ_p data displays a local s_2-minimum (=−0.15), found downstream in the same region as a local N_1-minimum (=−0.58); whilst for NM_τ_p_ABS these values appear at $\{s_2, N_1\} = \{-0.19, -0.64\}$. Finally, at the front-face of the contraction, a sharp negative N_1-peak is apparent for both {NM_τ_p, NM_τ_p_ABS}-fields, with values of $N_1 = \{-1.29, -0.92\}$, respectively. Consistently,

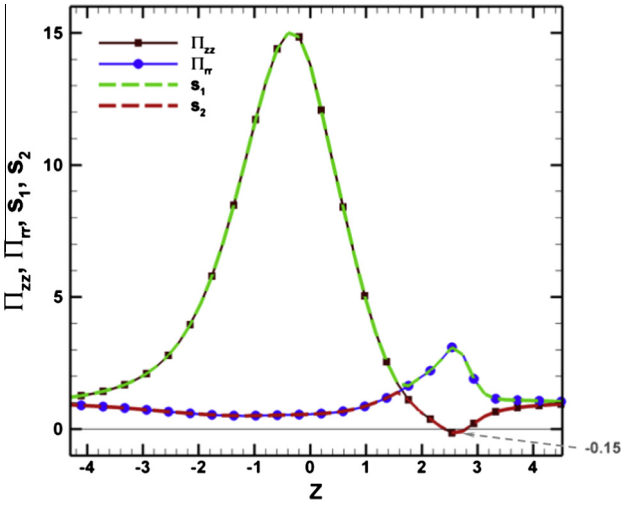

Fig. 3. Π_{zz}, Π_{rr}, s_1, s_2 at centreline; $We_{crit} = 4.9$; NM_τ_p.

N_{1max}-values decrease as the correction is implemented, with $N_{1max} = \{4.11_{wall}, 3.73\}$ for {NM_τ_p, NM_τ_p_ABS}. This reduction in N_1 peak values seems to be directly related with the extension in numerical instability, observed as the ABS-correction is implemented. Moreover, the location of this maxima change from the wall for NM_τ_p to the inner-field zone for NM_τ_p_ABS. This feature could be related to the change of shape of the red-positive zone in the 2D N_1-field across models: for NM_τ_p, a single region of positive values is apparent, whilst for NM_τ_p_ABS, two positive regions are observed; the largest attached to the centreline and reaching the tip of the contraction, and the second bulbous region detached from the back-face of the contraction.

5.3. We_{crit} levels

Table 3 lists critical Weissenberg number (over models and methods) according to the final stable solution-state (We_{crit}), and that at which solution breakdown (failure) is first detected (We_{fail}). For these micellar models, the inclusion of the ABS-correction generates an increase of some eight times in We_{crit}, from {$We_{crit} = 5$, NM_τ_p} to {$We_{crit} = 39$, NM_τ_p_ABS} representation. Generally, increasing f_τ-magnitude elevates the levels of computable We_{crit}-solutions [4] (down-scaling elasticity prominence). This is clearly the case when selecting the ABS-correction, and moreover, is exaggerated by selecting the absolute value of each individual component of the dissipation function (as opposed to the absolute value of the total dissipation function).

5.4. s_2 versus We history plot

Fig. 7 provides the detailed graphical data across models on s_{2min} as a function of *We*,[7] following Table 2. From the zoomed figure-inset in $0.1 \leqslant We \leqslant 0.5$ range, the NM_τ_p and NM_τ_p_ABS curves drop from $s_{2min} = 0.74$ at low elasticity levels ($We = 0.1$) and closely match, upholding the same declining trend up to $We = 0.5$. Subsequently for $We > 0.5$, the curves begin to depart from each other, with the NM_τ_p curve adopting the strongest negative declining slope. This is reflected in the precise *We* at which each data-curve crosses the zero-reference line. The NM_τ_p curve provides an intercept at $We \sim 1.4$, whilst the intercept for NM_τ_p_ABS curve is slightly retarded in this respect to $We \sim 1.6$. From this situation and from

[7] We_{inc}-NM_τ_p: unity to $We = 4$, in 0.1 to $We_{crit} = 4.9$; NM_τ_p_ABS: unity to $We = 10$, in 5 to $We = 30$, unity to $We_{crit} = 39$.

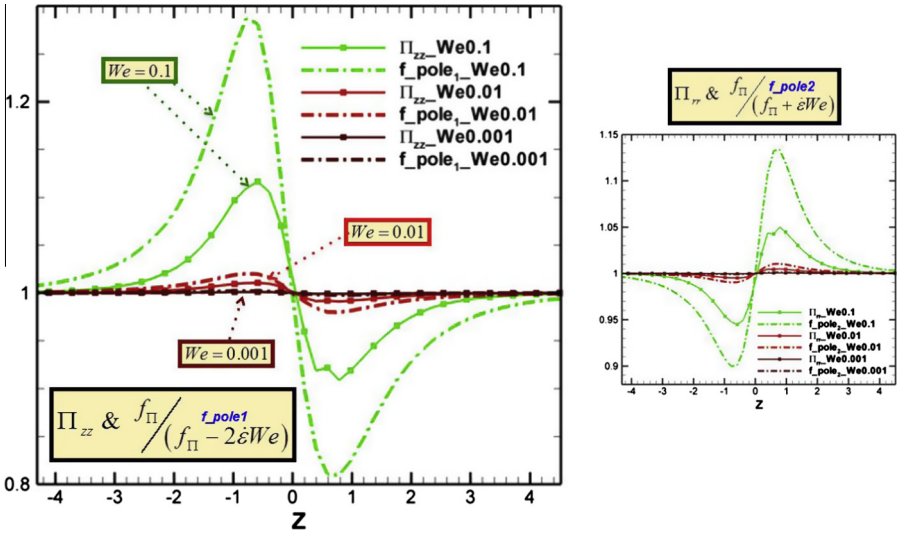

Fig. 4. Π_{zz}, linear-pole$_1$ estimation (inset Π_{rr}, linear-pole$_2$ estimation) at centreline. $We = \{0.001, 0.01, 0.1\}$; NM_$\tau_p$.

$We \geqslant 2$ onwards, NM_τ_p and NM_τ_p_ABS $s_{2\min}$-curves differ in solution gradient response, and markedly so for $We \geqslant 3$. The NM_τ_p curve gradually declines in slope in the interval $2 \leqslant We \leqslant 5$, locating drops with increasing magnitude at points $We = 3, 4$. Thereafter, for $We > 4$, the NM_τ_p curve declines most sharply, continuously and up to its $We_{\text{crit}} = 4.9$ state, with $s_{2\min} = -2.05$ now on the contraction-wall. In contrast and relative to NM_τ_p, the NM_τ_p_ABS $s_{2\min}$-curve adopts a continuous and shallow decline in slope which appears to reach a plateau in $3 \leqslant We < 20$ range (see full-scale plot). Around and after this $We = 20$ state, the NM_τ_p_ABS curve locates variation points at $We = \{20, 25, 30\}$, first declining less rapidly at $We = 20$, then more rapidly at $We = 25$, returning to less rapidly at $We = 30$, and continuing onwards towards $We_{\text{crit}} = 39$. At this critical solution stage, the negativity in s_2 has reached levels of $s_{2\min} = -143.55$. It is noteworthy that negativity in s_2 would appear to provide an over-strong indicator of primary solution quality, and indeed convergence to steady-state, as some degree of negativity in this factor is tolerated (under *We*-continuation, as opposed to IVP time-evolution, where the theory more strictly applies), whilst this does not hinder computation of smooth unpolluted solutions in all primary solution variables.

6. Highly elastic solutions

6.1. The VGR-correction – Micellar NM_τ_p_ABS_VGR model

6.1.1. We_{crit} levels

In addition to the ABS-correction and with the imposition of the enhanced centreline boundary conditions (NM_τ_p_ABS_VGR) as described in Section 2.4, converged steady-state solutions now become attainable at considerably higher Weissenberg numbers.[8] With reference to Table 3, an increase in We_{crit} level of some ten times is observed under NM_τ_p_ABS_VGR, relative to NM_τ_p_ABS capability. Specifically, NM_τ_p_ABS numerical solution breakdown is observed at $We_{\text{crit}} = 39$, whilst NM_τ_p_ABS_VGR attains the exaggerated response of $We_{\text{crit}} = 370$. This position is interrogated further below, through exposure to solution perturbation on the centreline via the deformation-gradients themselves, and hence the consistency of the problem. One notes, there is practically ***no change in f_τ-functional extrema*** between NM_τ_p_ABS and NM_τ_p_ABS_VGR; and hence, elevation in We_{crit} with NM_τ_p_ABS_VGR is attributed solely to the VGR-correction.

[8] We_{inc} – NM_τ_p_ABS_VGR: unity to $We = 10$, in 5 to $We = 200$, in 10 to $We_{\text{crit}} = 370$.

6.1.2. s_2 versus We history plot

Fig. 7 provides for comparison between NM_τ_p_ABS and NM_τ_p_ABS_VGR $s_{2\min}$-solution response, and emphasizes the more gradual/smoother changes gathered in the NM_τ_p_ABS_VGR $s_{2\min}$-curve up to and around $We_{\text{crit}} = 39$ for NM_τ_p_ABS. This theme is continued up to $We_{\text{crit}} = 370$, with essentially the same declining gradient trend after {NM_τ_p_ABS, $We_{\text{crit}} = 39$}; the refined deformation-gradient centreline conditions clearly provide for the advance in high *We*-number attenuation. One notes with look ahead, that the data on NM_$\boldsymbol{\Pi}$_ABS, is of similar form to that under NM_τ_p_ABS_VGR, displaying only slightly greater rate in $s_{2\min}$-decline beyond $We \sim 30$.

6.1.3. Deformation rates @ centreline

See Appendix B for detail on corresponding field data (Fig. B2). Fig. 8 graphs contrast NM_τ_p_ABS versus NM_τ_p_ABS_VGR data, for rising *We* and on the centreline, in shear du_z/dr and the extensional du_z/dz deformation gradient components. In Fig. 8a, there is conspicuous noise present in the *shear gradient* du_z/dr (NM_τ_p_ABS); absent under NM_τ_p_ABS_VGR, where the shear gradient vanishes. *Upstream* of the contraction, these NM_τ_p_ABS non-zero du_z/dr values tend to increase as *We* is elevated. Notably, at the axis $z = 0$, a minimum is observed for every *We*-data-curve; yet, the magnitude of this minimum is rising for $0.1 \leqslant We \leqslant 5$, whilst decreasing for $We \geqslant 10$. *Downstream* of the contraction, du_z/dr-data-curves reflect rather oscillatory behaviour, adopting a damped pattern with *We* rise, somewhat resembling the convected patches in N_1 and s_2-fields (Fig. 8a and b). In contrast, data-curves under NM_τ_p_ABS_VGR (Fig. 8b) display null du_z/dr at the centreline. In terms of normal gradient component representation, *extensional rate* du_z/dz data is imposed on the other two normal components, discretely conveyed through du_r/dr approximation (Fig. 8c and d). VGR-correction at $We = \{2, 5\}$ is evident, through localised differences and their subsequent downstream convection; this may be gathered in the comparison between data-curves in NM_τ_p_ABS and NM_τ_p_ABS_VGR solutions downstream of the contraction. Relatively smoother trends in du_r/dr curves are observed under the (pink) NM_τ_p_ABS_VGR data-curve. Conspicuously, adjustments in the shear du_z/dr component prove to be an order of magnitude larger than those in the extensional du_r/dr component.

6.1.4. Stress fields – solution quality

Fig. B1(ii) gathers VGR-correction data in N_1, s_2, τ_{rz} and N_2 2D-fields, with rising *We* and sampled at incremental stages. Between

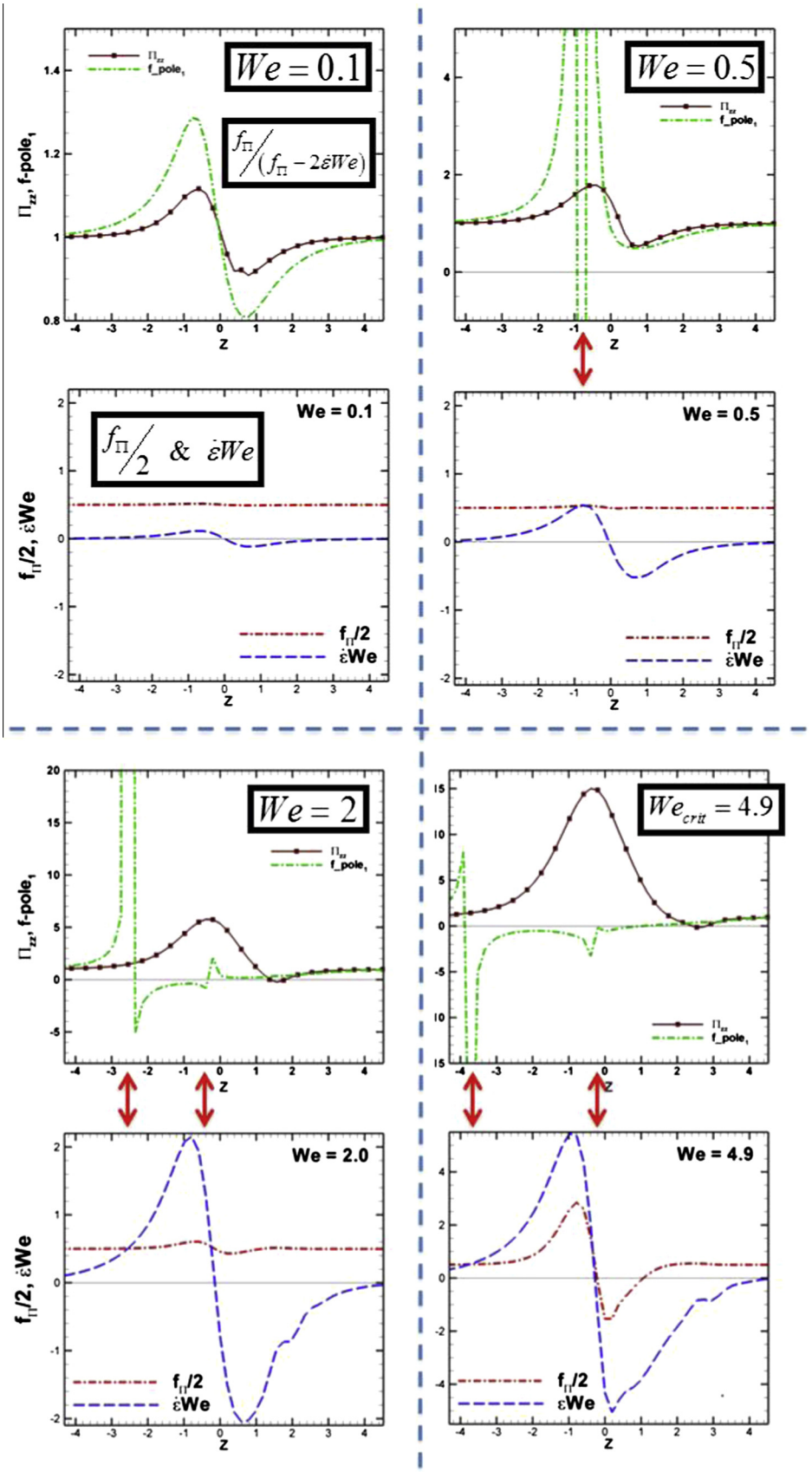

Fig. 5. Π_{zz}, linear-pole$_1$ estimation and pole$_1$-components at centreline. $We = \{0.1, 0.5, 2, 4.9\}$; NM_$\tau_p$.

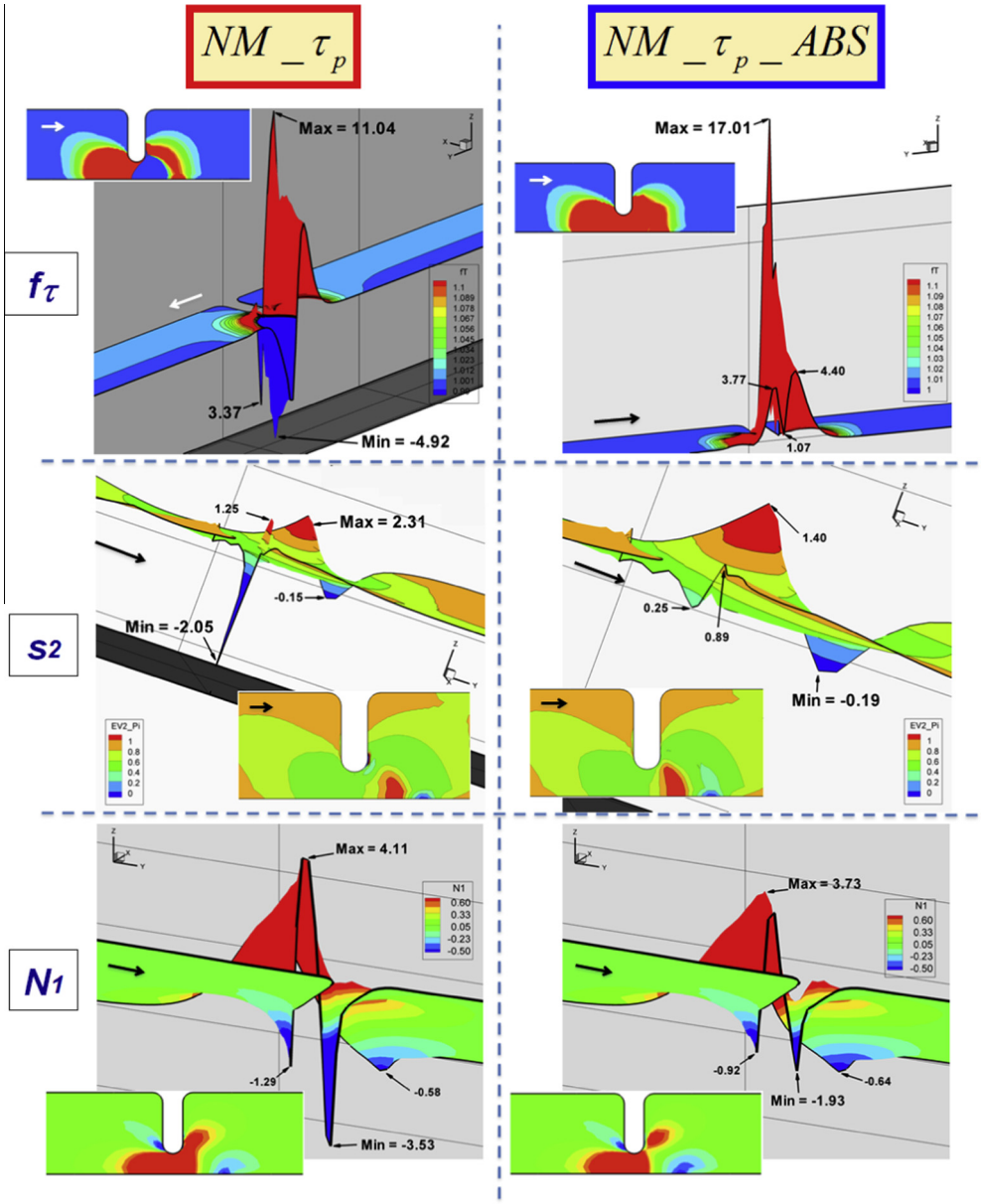

Fig. 6. f_τ-functional, s_2 and N_1 2D, 3D-fields at $We = 4.9$; NM_τ_p and NM_τ_p_ABS.

Table 3
{Critical, first-failure} Weissenberg numbers {We_{crit}, We_{fail}} across models.

Model	f_τ	We_{crit} (We_{fail})			
		Natural Sign	ABS	VGR	Π
NM_τ_p	$1+\omega\xi_{C_0}We\tau_p : D$	4.9 (5)	39 (40)	370 (380)	175 (180)
LPTT	$1+\frac{\varepsilon We}{1-\beta}tr\tau_p$	11 (12)	210 (220)	–	–
EPTT	$\exp\left(\frac{\varepsilon We}{1-\beta}tr\tau_p\right)$	210 (220)	4000 (4250)	4250 (4500)	1000 (1250)

NM_τ_p_ABS (Fig. B1(i)) and NM_τ_p_ABS_VGR Fig. B1(ii) solutions up to $We \sim 40$, there are no noticeable solution differences in f_τ-fields or other variables. Of the **N_1-field** in the $75 < We < 370$ range (Fig. B1(ii)a), the most significant feature lies in the red-positive downstream-zone that originated from the second bulbous-zone in Fig. B1(i)a and split off downstream around $We \sim 20$; this has now further elongated downstream and parallel to the channel-wall, passing incrementally in steps through $We = \{40, 75, 175, 370\}$, with signs of splitting about its centre around $We \sim 175$. This has certainly occurred at the advanced stage of $We_{crit} = 370$. Similarly in the same We-range and on **τ_{rz}-field** data, the downstream obstruction-backface detached-satellite red-positive zone (from $We \sim 20$, Fig. B1(ii)c) is continuously convected with rising We along the obstruction face towards the salient vortex region and becoming more intense. The **N_2-field** data continues to convey the signature of vortex activity in the

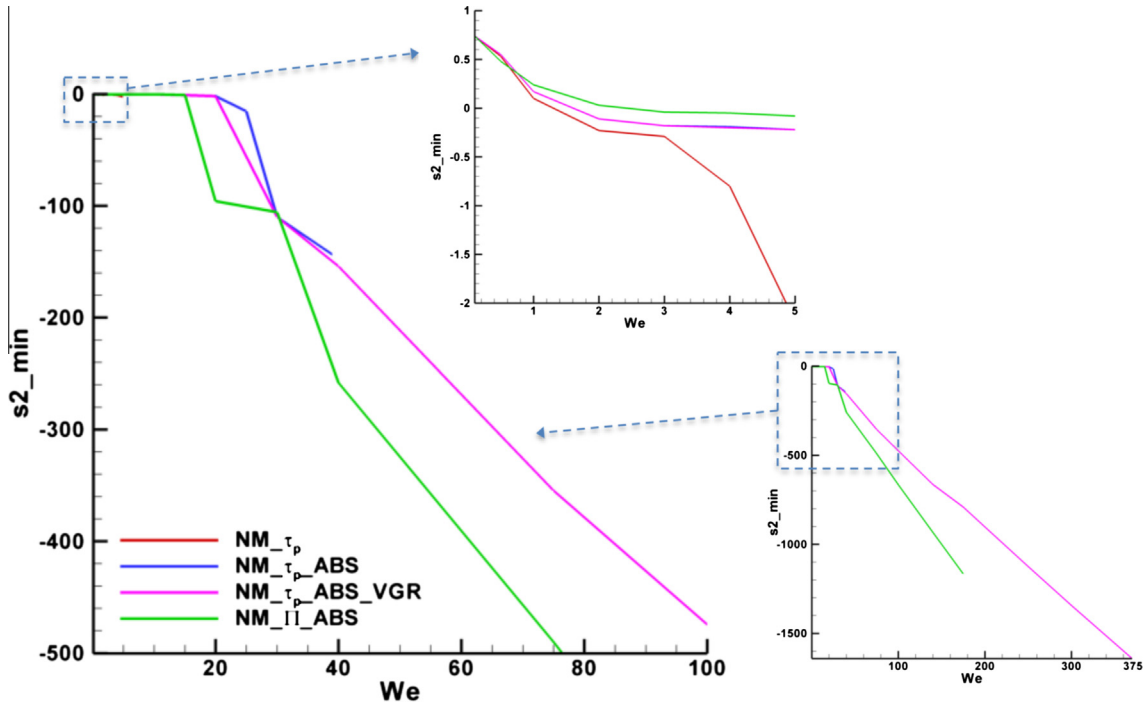

Fig. 7. $s_{2\min}$ versus *We*; NM_τ_p, NM_τ_p_ABS, NM_τ_p_ABS_VGR and NM_$\boldsymbol{\Pi}$_ABS.

upstream salient corner of Fig. B1(i)d [4], increasing upstream in Fig. B1(ii)d up to $We \sim 175$; strain-softening eventually provides some slight shrinkage of this structure, apparent at $175 < We < 370$. One notes ahead that the equivalent stress-data on micellar NM_$\boldsymbol{\Pi}$_ABS (Fig. B1(iii)), largely replicates that of NM_τ_p_ABS_VGR; only noting clearer downstream splitting of the N_1 red-zone earlier around $We \sim 75$, and less intense structures on the downstream obstruction-backface.

6.2. Conformation-tensor solutions – Micellar NM_$\boldsymbol{\Pi}$_ABS model

6.2.1. We_{crit} levels

In addition to the ABS-correction, this second strategy to attain high-*We* solutions focuses on solving the problem when cast in primary variable conformation tensor form (see Eqs. (8)–(10)). The critical elasticity level attainable with NM_$\boldsymbol{\Pi}$_ABS is $We_{\text{crit}} = 175$ (Table 3),[9] which stands at some 4.5 times that achieved with NM_τ_p_ABS. Hence, as proposed in theory, the posing of the problem through its corresponding differential constitutive equation (with its data dependency) and its boundary conditions, does discretely have an impact on tractability of numerical solutions. Moreover, the constitutive equation solved for each case plays an important role, since the $\boldsymbol{\Pi}$-based equation is reinforced relative to the $\boldsymbol{\tau}_p$-based equation, maintaining positive definiteness via (i) $f_{\boldsymbol{\Pi}}$ acting as a RHS-equation scaling-factor, and (ii) the explicit absence of the rate-of-deformation tensor $\boldsymbol{D}$. Consistently, $f_{\boldsymbol{\Pi}}$-*functional* values originating from NM_$\boldsymbol{\Pi}$_ABS are larger compared with the remaining τ_p-versions (Table 1) [4]. In contrast to the further achievements with $\boldsymbol{\Pi}$-VGR-correction, one can state that this position is not substantially altered under combination with the conformation tensor implementation (as in NM_$\boldsymbol{\Pi}$_ABS_VGR). It is conspicuous that NM_τ_p_ABS_VGR capability in this regard outperforms the {NM_$\boldsymbol{\Pi}$_ABS, $We_{\text{crit}} = 175$} implementation, with the exaggerated response of {NM_τ_p_ABS_VGR, $We_{\text{crit}} = 370$}.

[9] We_{inc}–NM_$\boldsymbol{\Pi}$_ABS: analogous to NM_τ_p_ABS_VGR with earlier $We_{\text{crit}} = 175$.

Hence, though the conformation tensor approach is certainly a reasonable candidate to consider for generating high-*We* steady-state solutions, one concludes thus far and in practical terms, that the superior method of implementation is VGR-correction imposed on NM_τ_p_ABS.

7. General applicability – PTT($\varepsilon = 0.25$, $\beta = 1/9$) solutions: EPTT and LPTT results

7.1. We_{crit} levels

In an effort to assess more widely the generality and applicability of current findings to cover alternative constitutive models, one may appeal to the class of Phan–Thien–Tanner models, being non-thixotropic and phenomenological viscoelastic models derived from a network-basis. Table 3 lists counterpart high We_{crit} findings for such model solutions, under application of ABS, VGR and $\boldsymbol{\Pi}$-corrections, as above. These are now impressively large, unrealised elsewhere, and offer wide scope for new application accordingly (large deformation scenarios, as in microfluidics). Conspicuously, the ABS-correction yields an order-of-magnitude increase in We_{crit}, from $O(10^2)$ under the natural-signed version [4], to $O(10^3)$ under EPTT_ABS results. Specifically, $We_{\text{crit}} = 210$ for the natural signed EPTT model [4], has now been further increased to $We_{\text{crit}} = \{4000, 4250, 1000\}$ for {EPTT_ABS, EPTT_ABS_VGR, EPTT_ABS_Π}.[10] Consistently to the thixotropic context above with $\boldsymbol{\Pi}$-correction, which also subsumes ABS-correction, there is improvement in We_{crit} of some five-times above the natural-signed EPTT_τ_p alternative; yet, this lies some four times lower than that achieved under EPTT_ABS and EPTT_ABS_VGR counterparts. Note, the level of $We_{\text{crit}} = 210$ for the natural-signed EPTT model [4], is already elevated above that for thixotropic NM_τ_p, (see also $We_{\text{crit}} = 11$ for natural-signed linear-version LPTT). As previously reported elsewhere [4], such

[10] We_{inc}–EPTT_ABS, EPTT_ABS_VGR and EPTT_ABS_$\boldsymbol{\Pi}$: analogous to NM_τ_p_ABS_VGR to $We = 400$, in 50 to $We = 500$, in 250 to corresponding We_{crit}.

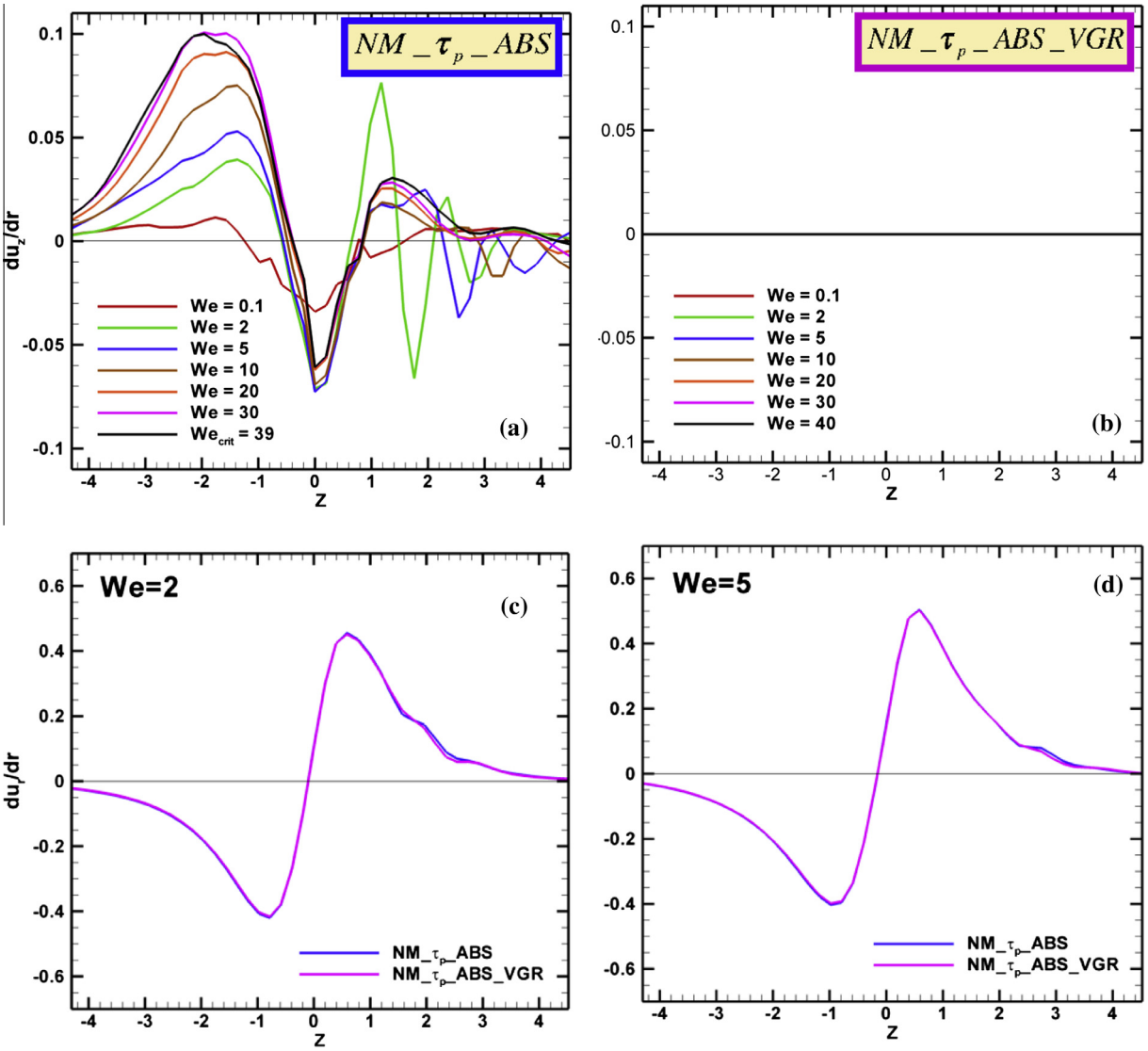

Fig. 8. At centreline: (a) and (b) du_z/dr versus *We*; du_r/dr (c) *We* = 2 and (d) *We* = 5. NM_τ_p_ABS and NM_τ_p_ABS_VGR.

high-*We* solutions attainable with EPTT versions, are in part a consequence of its non-linear exponential explicit f_τ-*We* functionality (Eq. (7)). In contrast, linear f_τ-*We* relationships are observed within steady-state f_τ for thixotropic NM_τ_p (Eq. (5)) models or non-thixotropic LPTT version. This is reflected in complex flow via the relatively large EPTT f_τ-maxima encountered as *We* is elevated and when compared to those under NM_τ_p (or LPTT) solutions (Table 1).

7.2. Considerations at very high-We levels

Fig. 9 gathers a sample of high-*We* EPTT_ABS solutions, via the stress discriminant in the expression for the eigenvalues, s_1 and s_2 (Eqs. (18) AND (19)). Here a fresh phenomenon arises, not prominent at more moderate *We*-levels. At such large *We* = O(10^3) levels, numerical noise becomes evident in the solution exit-zone (Fig. 9a), which is first detected around *We* ∼ 750 cross-stream and emanating from the centreline. This feature, which grows with further rise in *We*, comes from solution anomalies arising between interior domain and boundary section solution approximation (applies similarly at inlet-station, 1000 < *We* < 2000). These *theoretic-discrete* inlet–outlet region considerations are not graphically evident at relatively low *We* < 220; they onset earlier at exit than entry at *We* ∼ 750; strengthen at exit *We* ∼ 1000; become strong and clearly manifested around *We* ∼ 2000, at inlet and outlet; to be finally, amplified as *We* rises up to We_{crit} = 4000, when inlet fluctuations are apparent and penetrating into the field up to the contraction itself. These inconsistencies are dealt with by a feedback–feedforward technique on stress/kinematics, to mimic steady fully-developed flow state, taking primary information from the interior-domain discrete solution and translating this to the domain boundary sections. This is accomplished by averaging internal stress/velocity-gradient components (velocity remains unadjusted) and substituting this refreshed information into inlet and outlet neighbour nodal points, to thus reset the stress components. Implementation of such a procedure, removes the source of solution discrepancy arising at inlet–outlet, to provide the counterpart and repaired solution forms of Fig. 9b, which have been extended to even larger *We*-levels (*We* = 5000+).

8. Conclusions

Highly elastic thixotropic solutions have been achieved through three alternative approaches (independent, interchangeable): (i) absolute f_τ-functional correction (ABS-correction – related to

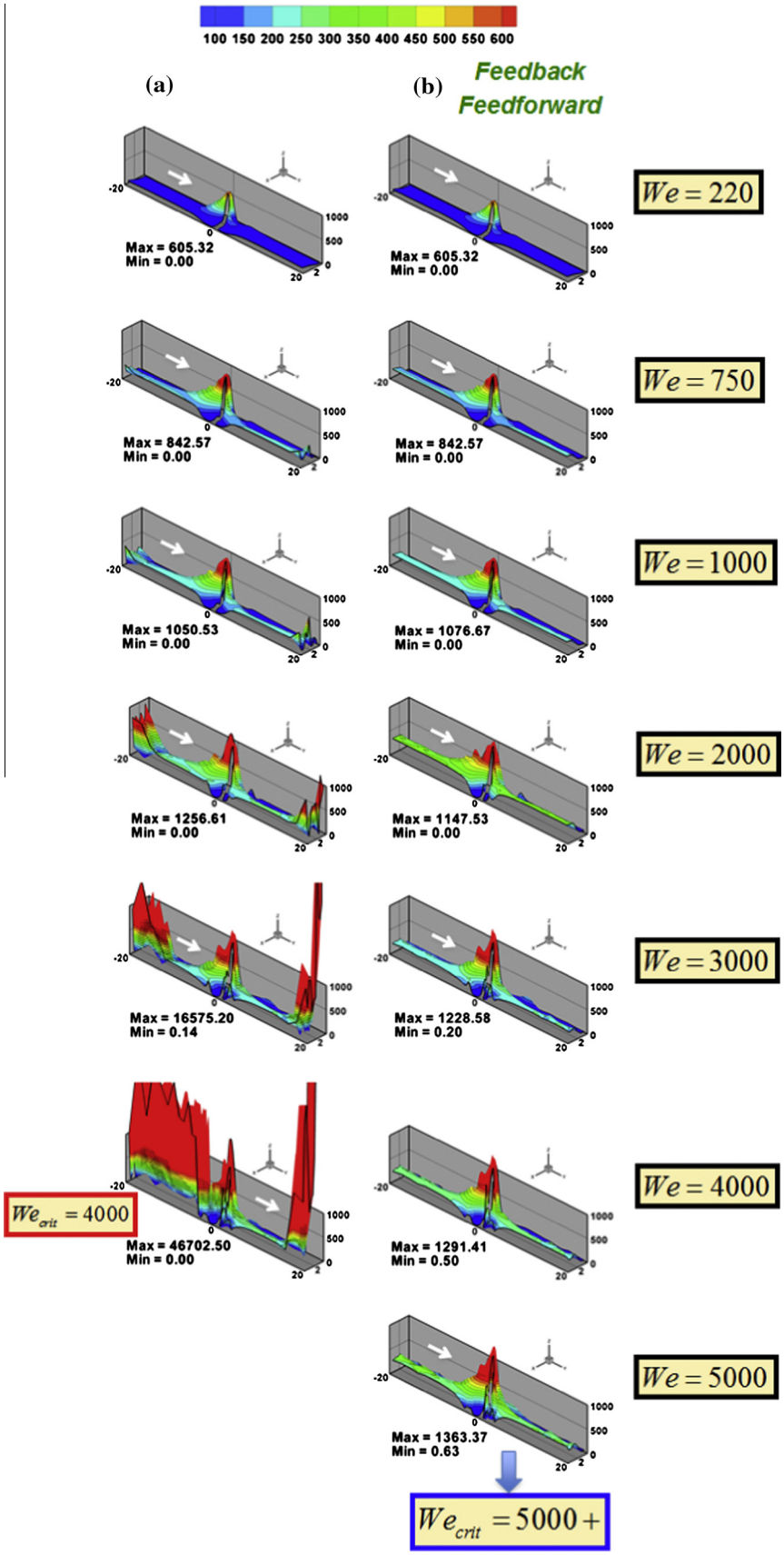

Fig. 9. Stress discriminant fields versus *We*; EPTT and EPTT_ABS.

positive energy dissipation [32] and accurate viscosity prediction); (ii) centreline velocity gradient correction (VGR-correction – f_τ-values as with ABS-correction); (iii) $\boldsymbol{\Pi}$ conformation tensor correction ($\boldsymbol{\Pi}$-correction – change of variable). The first two alternatives have provided an increase of some ten times in We_{crit} on their preceding versions. ABS-correction adjusts {We_{crit} = 4.9, NM_τ_p} to {We_{crit} = 39, NM_τ_p_ABS}; whilst VGR-correction renders {NM_τ_p_ABS_VGR, We_{crit} = 370} layered on top of ABS-correction. The third alternative {NM_$\boldsymbol{\Pi}$_ABS, We_{crit} = 175} has also increased We_{crit} by some five times with respect to NM_τ_p_ABS solutions.

The s_2-eigenvalue has been identified as a suitable marker for numerical stability retention. Localised minima first arise on the centreline, just downstream of the contraction, which are found responsible for linking-up and stimulating contraction-wall minima, that ultimately dominate overall as *We* rises. Then, localised undershoot–overshoot phenomena (reflected in N_1 and *f*-functional data) are observed on the backface of the contraction-wall, with subsequent solution penetration into the field. The ABS-correction retards the appearance of such s_2 undershoot–overshoot phenomena, although ultimately their presence does not affect the quality of solutions in primary variables. This is noted through smooth and tractable trends in $\{\tau_{rz}, N_1, N_2\}$-fields and *We*-incrementation. N_2 provides insight on trends in upstream vortex-dynamics with *We* elevation [4]: reflecting initial vortex-enhancement, then, vortex-suppression {NM_τ_p_ABS_VGR, 175 < *We* < 370}.

Theoretical observations are derived on $\boldsymbol{\Pi}$-component response under centreline deformation conditions. This is detailed through *We* rise via: (i) $\{s_1, s_2\}$ eigenvalue-pair dual-nature in correspondence with $\{\boldsymbol{\Pi}_{zz}, \boldsymbol{\Pi}_{rr}\}$; (ii) location of discontinuities in the linearised inhomogeneous $\boldsymbol{\Pi}$-component estimation, interpreted against the components of its poles; and (iii) numerical $\{\boldsymbol{\Pi}_{zz}, \boldsymbol{\Pi}_{rr}\}$ departure from their linearised inhomogeneous estimation. In the first aspect this relies upon $\{s_1, s_2\}$ eigenvalue-pair dual-nature being dictated by the sign-switch in N_1. The third aspect dictates the degree and capture of departure from the linear viscoelastic regime.

In addition, generalisation of current findings for thixotropic theory has been explored under classical non-thixotropic models too. This has led to incrementation in We_{crit} well over an order of magnitude for network-based time-independent PTT models (ABS-correction relates to positive stored elastic energy in this case [21]); in contrast to two orders of magnitude achieved for thixotropic models. Stable solutions have been extended for the *exponential*-PTT version, from the natural-signed {EPTT, We_{crit} = 230} to {EPTT_ABS, We_{crit} = 4000}; and {EPTT_ABS_VGR, We_{crit} = 4250}. In its conformation-tensor form, incrementation is observed with {EPTT_ABS_$\boldsymbol{\Pi}$, We_{crit} = 1000}. In terms of the *linear*-PTT version, the natural-signed {LPTT, We_{crit} = 11} is now adjusted to {LPTT_ABS, We_{crit} = 210}. The relatively larger We_{crit} under EPTT are due to its larger f_τ-values, coming from its exponential f_τ–*We* relationship, as opposed to those under the linear relationship given with LPTT and NM_τ_p models [4]. At very high *We* = O(10^3) and for EPTT, it has been shown how to ensure satisfaction of fully-developed inlet–outlet region conditions (theory to practice, avoiding inlet–outlet inconsistencies), to ultimately gather smooth solutions at even larger elasticity levels (*We* = 5000+).

Acknowledgements

Financial support (scholarship to J.E.L.-A.) from Secretaría de Educación Pública (SEP, México), Zienkiewcz College of Engineering scholarship and NHS-Wales Abertawe Bro Morgannwg Trust-fund, is gratefully acknowledged.

Appendix A

A.1 $\boldsymbol{\Pi}$-eigenvalues at the centreline (shear-free flow)

The eigenvalues of the $\boldsymbol{\Pi}$-tensor at the centreline reveal some interesting properties, worthy of further inspection. Shear-free flow applies along this flow-line ($\boldsymbol{\Pi}_{rz} = 0$), and hence, Eqs. (15) and (16) reduce to:

$$(\Pi_{zz} - s)(\Pi_{rr} - s) = 0, \tag{A.I}$$

$$s^2 - (\Pi_{zz} + \Pi_{rr})s + (\Pi_{zz}\Pi rr) = 0. \tag{A.II}$$

The discriminant associated with the solution of Eq. (A.II) is:

$$(\Pi_{zz} + \Pi_{rr})^2 - 4\Pi_{zz}\Pi_{rr} = (\Pi_{zz}^2 + 2\Pi_{zz}\Pi_{rr} + \Pi_{rr}^2) - 4\Pi_{zz}\Pi_{rr} = \Pi_{zz}^2 - 2\Pi_{zz}\Pi_{rr} + \Pi_{rr}^2,$$

viz,

$$(\Pi_{zz} + \Pi_{rr})^2 - 4\Pi_{zz}\Pi_{rr} = (\Pi_{zz} - \Pi_{rr})^2 = N_1^2$$

From which the eigenvalues are then given by:

$$\{s_1, s_2\} = \frac{\Pi_{zz} + \Pi_{rr} \pm |N_1|}{2} \tag{A.III}$$

With dependence on the sign-switch of N_1 on the centreline, three instances can be identified from Eq. (A.III):

(a) when $N_1 > 0 \rightarrow N_1 = \boldsymbol{\Pi}_{zz} - \boldsymbol{\Pi}_{rr}$, $s_1 = \boldsymbol{\Pi}_{zz}$, $s_2 = \boldsymbol{\Pi}_{rr}$;
(b) $N_1 = 0 \rightarrow \boldsymbol{\Pi}_{zz} = \boldsymbol{\Pi}_{rr}$, $s_1 = \boldsymbol{\Pi}_{zz} = s_2 = \boldsymbol{\Pi}_{rr} = tr\boldsymbol{\Pi}^{\text{sub}}/2$;
(c) when $N_1 < 0 \rightarrow N_1 = \boldsymbol{\Pi}_{rr} - \boldsymbol{\Pi}_{zz}$, $s_1 = \boldsymbol{\Pi}_{rr}$, $s_2 = \boldsymbol{\Pi}_{zz}$.

Hence, theoretically on the centreline, a duality exists in the nature of the component identities between the $\{s_1, s_2\}$ eigenvalue pairs, and is dictated by the sign-switch in the first normal stress difference at this shear-free flow-line. What is clear is that each eigenvalue here picks up the identity of the local $\boldsymbol{\Pi}_{ii}$ component, and that this tensor component switches over its roll of eigenvalue dependency as the sign-switch in N_1 is traversed. Hence, both eigenvalues have an intimate roll to play in the analysis. Universal findings, to be discussed subsequently below, reveal that the corresponding centreline pattern of behaviour taken up by $\{s_1, s_2\}$ is such that s_1 remains positive $\forall z$, whilst s_2 has the potential to decline into minor negativity, subject to a number of constraints. Hence, it is s_2-response that is particularly instructive to focus attention on below.

A.2. $\boldsymbol{\Pi}$-eigenvalue relationship with f-functional poles in simple uniaxial extension

Consideration of simple uniaxial extension (or compression) within Eq. (8) under deformation rate $\dot{\varepsilon}$, applicable to the linear viscoelastic regime, realises:

$$\overset{\nabla}{\Pi} = -2\begin{bmatrix} \dot{\varepsilon}\Pi_{zz} & 0 & 0 \\ 0 & \left(-\frac{\dot{\varepsilon}}{2}\right)\Pi_{rr} & 0 \\ 0 & 0 & \left(-\frac{\dot{\varepsilon}}{2}\right)\Pi_{\theta\theta} \end{bmatrix}, \tag{A.IV}$$

from which one extracts solutions of the form:

$$\Pi = \begin{bmatrix} f_\Pi/(f_\Pi - 2We\dot{\varepsilon}) & 0 & 0 \\ 0 & f_\Pi/(f_\Pi + We\dot{\varepsilon}) & 0 \\ 0 & 0 & f_\Pi/(f_\Pi + We\dot{\varepsilon}) \end{bmatrix}. \tag{A.V}$$

Hence and from the above analysis, the first and second eigenvalues on the centreline, in non-homogeneous uniaxial extension, may be approximated by $s_1 = \Pi_{zz} = f_\Pi/(f_\Pi - 2We\dot{\varepsilon})$ and $s_2 = \Pi_{rr} = f_\Pi/(f_\Pi + We\dot{\varepsilon})$. This equivalence holds exactly in the linear viscoelastic regime and for homogeneous extension conditions.

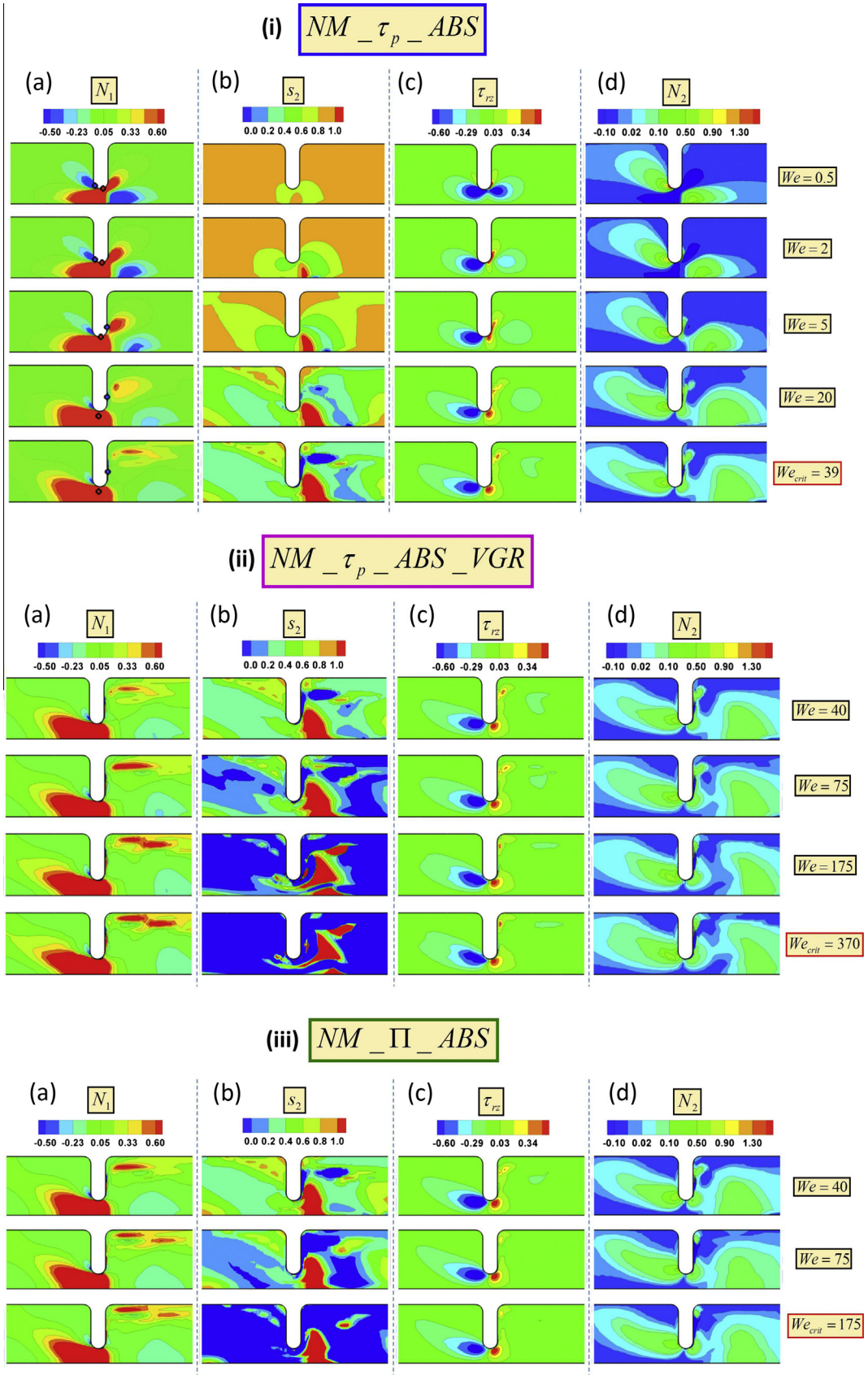

Fig. B1. N_1, s_2, τ_{rz}, N_2 2D-fields versus *We*; (i) NM_τ_p_ABS, (ii) NM_τ_p_ABS_VGR and (iii) NM_Π_ABS.

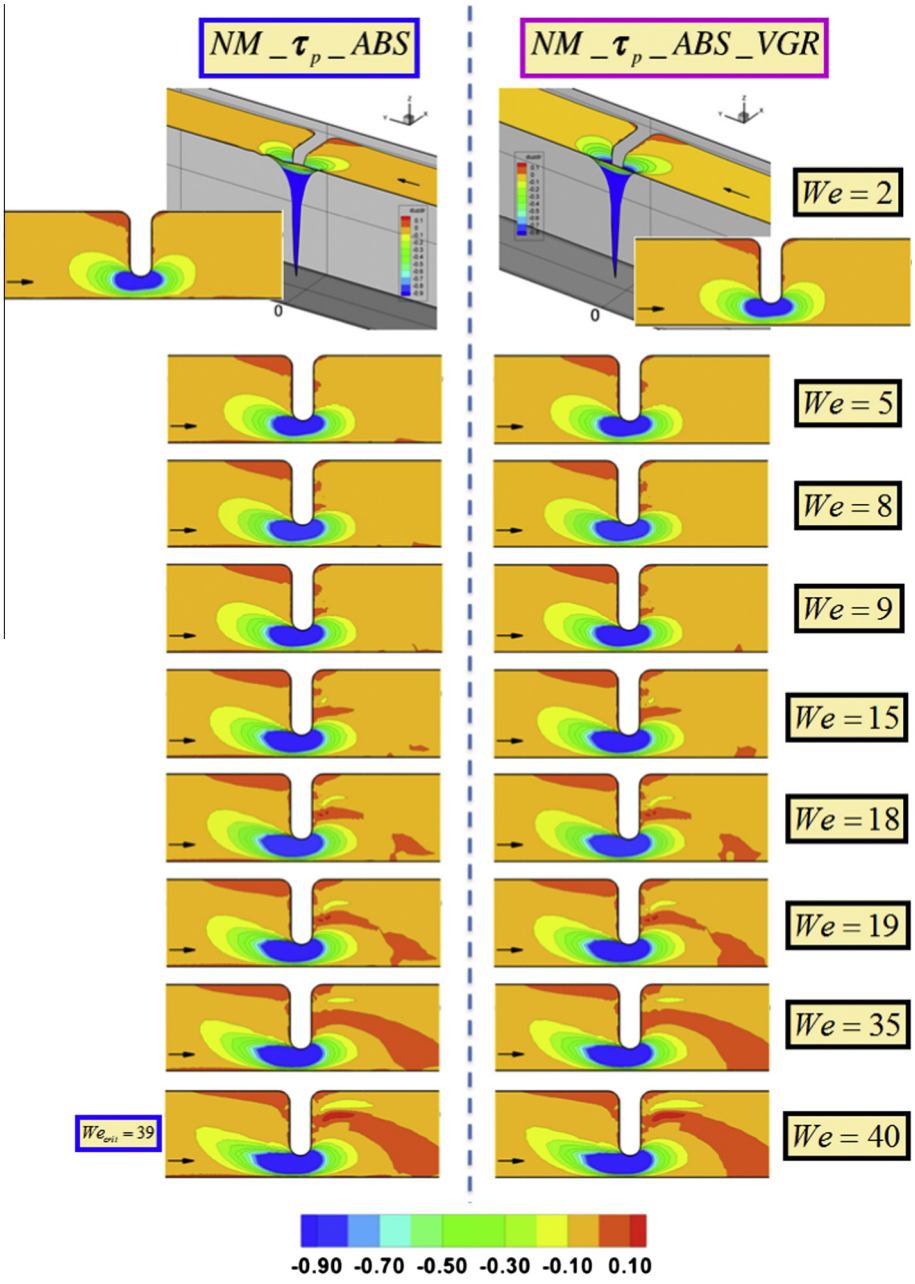

Fig. B2. $du_z dr$ 2D, 3D-fields versus *We*; NM_τ_p_ABS and NM_τ_p_ABS_VGR.

Hence, one may identify departure in numerical solutions generated under inhomogeneous extensional conditions, and indeed the various windows of influence of departure from fully-developed flow.

Appendix B

B.1. Stress fields – solution quality

Fig. B1(i) gathers together comparatively a sample of stress data for the NM_τ_p_ABS model, via *first* (and *second*) *normal stress-difference* N_1 (and N_2), *shear stress* τ_{rz} and *second eigenvalue* s_2-data (2D-fields) at selected $We = \{0.5, 2, 5, 39\}$. Notably, these N_1 and τ_{rz} 2D-fields display continuous change through *We* incrementation, without evidence of numerical pollution (see Section 5.4 for identification of eigenvalues, positive-definiteness). More sporadic field patterns become apparent in s_2-data and $We > 40$, useful to hold comparatively against the stress data. Particularly on N_1 (Fig. B1(i)a) at $We = 0.5$, regions with positive (red) and negative (blue) values can be identified, with extrema indicated of $\{N_{1\max} = 4.48,\ N_{1\min} = -2.49\}$. At $We = 2$ and under greater influence of shear-thinning/extension-softening, these extrema have diminished in magnitude to $\{N_{1\max} = 4.20,\ N_{1\min} = -1.47\}$. At $We = 5$ stage (NM_τ_p $We_{crit} = 4.9$), N_1-extrema continue to decrement, with $\{N_{1\max} = 3.73,\ N_{1\min} = -1.92\}$. Importantly at $We_{\text{crit}} = 39$, there is evidence of overshoots–undershoots in N_1 attached to the obstruction downstream backface-wall, as a new and third positive-region has emerged, located alongside the third blue-region (now larger and more conspicuous than before). Notably, this local behaviour correlates to $s_{2\min}$ negative-extremum. N_1-extrema at this critical stage are smallest reported, with $\{N_{1\max} = 3.67,\ N_{1\min} = -1.76\}$. N_2-data with rising *We* is also included, to indicate trends in vortex region activity (see NM_τ_p

in [4] up to $We_{crit} = 4.9$), where upstream growth is apparent (deep-blue zone) and sustained through increasing *We*; whilst only vortex decay is displayed downstream (absent by $We = 2$). In Fig. B1(i)c, comparable τ_{rz}-field response is less dramatic than in N_1. In the τ_{rz}-field at $We = 0.5$, τ_{rz}-extrema are largest reported at $\{\tau_{rzmax} = 1.54,\ \tau_{rzmin} = -1.77\}$; diminishing by $We = 2$ to $\{\tau_{rzmax} = 1.28,\ \tau_{rzmin} = -1.10\}$, due to greater shear-thinning. Furthermore at $We = 5$, even greater shear-thinning effects render reduced extrema of $\{\tau_{rzmax} = 0.91,\ \tau_{rzmin} = -0.94\}$. Proceeding to $We_{crit} = 39$; the most prominent feature to report is the splitting of the second-downstream red-positive region (already apparent at $We = 20$), leaving a zone located above the obstruction backface-tip and a satellite zone that has drifted off downstream, periphery to the downstream-vortex region; τ_{rz}-extrema are now least in magnitude, being $\{\tau_{rzmax} = 0.66,\ \tau_{rzmin} = -0.84\}$.

B.2. Shear deformation rate fields

In Fig. B2 du_z/dr 3D and 2D-fields are contrasted for NM_τ_p_ABS versus NM_τ_p_ABS_VGR at rising *We*. Elimination of noise proliferation under VGR-correction is clearly observed in the undulating centreline patterns in the du_z/dr 3D-NM_τ_p_ABS solutions at every elasticity instance (shown for $We = 2$). These centreline undulations (in $du_z/dr \neq 0$) are convected downstream of the contraction as *We* is elevated, although there is evidence here for the continued persistence of these undulations in the contraction-gap itself on the centreline (permanent deformation) and via upstream field-penetration. In contrast, for NM_τ_p_ABS_VGR solutions, this flow-line remains unperturbed throughout the *We*-continuation process. Moreover for $We \geqslant 2$, signals of pollution in NM_τ_p_ABS solutions are evident off the centreline, upstream and downstream of the contraction; whilst NM_τ_p_ABS_VGR fields remain unpolluted up to $We = 8$. Some solution gradient activity is becoming apparent on the backface obstruction-wall at $We = 5$ (more prominent at $We = 9$), for both NM_τ_p_ABS and NM_τ_p_ABS_VGR. This is manifest through *three locations*: one located at the centre of the obstruction-wall and the other two near its extremities, in the salient and corner-tip neighbourhoods. Through *We*-rise, the most influential of these three is that near the tip of the obstruction. This feature continues to grow downstream penetrating the field, and subsequently links up in a stalagmite–stalactite fashion to its counterpart downstream, just-off-centreline, positive growth-point, uniting at $We = 19$. The growth pattern of this positive-point is: first appears at {$We = 5$, NM_τ_p_ABS} and {$We = 9$, NM_τ_p_ABS_VGR}; with a distinct gap to centreline under NM_τ_p_ABS.

References

[1] F. Bautista, J.M. de Santos, J.E. Puig, O. Manero, Understanding thixotropic and antithixotropic behavior of viscoelastic micellar solutions and liquid crystalline dispersions. I. The model, J. Non-Newton. Fluid Mech. 80 (1999) 93–113.

[2] O. Manero, F. Bautista, J.F.A. Soltero, J.E. Puig, Dynamics of worm-like micelles: the Cox–Merz rule, J. Non-Newton. Fluid Mech. 106 (2002) 1–15.

[3] E.S. Boek, J.T. Padding, V.J. Anderson, P.M.J. Tardy, J.P. Crawshaw, J.R.A. Pearson, Constitutive equations for extensional flow of wormlike micelles: stability analysis of the Bautista–Manero model, J. Non-Newton. Fluid Mech. 126 (2005) 29–46.

[4] J.E. López-Aguilar, M.F. Webster, H.R. Tamaddon-Jahromi, O. Manero, A new constitutive model for worm-like micellar systems – numerical simulation of confined contraction-expansion flows, J. Non-Newton. Fluid Mech. 204 (2014) 7–21.

[5] F. Calderas, E.E. Herrera-Valencia, A. Sanchez-Solis, O. Manero, L. Medina-Torres, A. Renteria, G. Sanchez-Olivares, On the yield stress of complex materials, Korea-Aust. Rheol. J. 25 (2013) 233–242.

[6] J. Yang, Viscoelastic wormlike micelles and their applications, Curr. Opin. Colloid Interface Sci. 7 (2002) 276–281.

[7] H.R. Tamaddon-Jahromi, M.F. Webster, J.P. Aguayo, O. Manero, Numerical investigation of transient contraction flows for worm-like micellar systems using Bautista–Manero models, J. Non-Newton. Fluid Mech. 166 (2011) 102–117.

[8] P.A. Vazquez, G.H. McKinley, L.P. Cook, A network scission model for wormlike micellar solutions I. Model formulations and viscometric flow predictions, J. Non-Newton. Fluid Mech. 144 (2007) 122–139.

[9] P.D. Olmsted, O. Radulescu, C.Y.F. Lu, Johnson–Segalman model with a diffusion term in a cylindrical Couette flow, J. Rheol. 44 (2000) 257–275.

[10] A.K. Gurnon, N.J. Wagner, Large amplitude oscillatory shear (LAOS) measurements to obtain constitutive equation model parameters: Giesekus model of banding and nonbanding wormlike micelles, J. Rheol. 56 (2012) 333–351.

[11] X.F. Yuan, L. Jupp, Interplay of flow-induced phase separations and rheological behavior of complex fluids in shearbanding flow, Europhys. Lett. 60 (2002) 691–697.

[12] J.Y. Lee, G.G. Fuller, N.E. Hudson, X.F. Yuan, Investigation of shear-banding structure in wormlike micellar solution by point-wise flow-induced birefringence measurements, J. Rheol. 49 (2005) 537–550.

[13] K. Walters, M.F. Webster, The distinctive CFD challenges of computational rheology, Int. J. Numer. Meth. Fluids 43 (2003) 577–596.

[14] R. Keunings, On the high Weissenberg number problem, J. Non-Newton. Fluid Mech. 20 (1986) 209–226.

[15] F.T.P. Baaijens, Mixed finite element methods for viscoelastic flow analysis: a review, J. Non-Newton. Fluid Mech. 79 (1998) 361–385.

[16] R. Keunings, Advances in the computer modeling of the flow of polymeric liquids, Comp. Fluid Dyn. J. 9 (2001) 449–458.

[17] F. Dupret, J.M. Marchal, M.J. Crochet, On the consequence of discretization errors in the numerical calculation of viscoelastic flow, J. Non-Newton. Fluid Mech. 18 (1985) 173–186.

[18] F. Dupret, J.M. Marchal, Loss of evolution in the flow of viscoelastic fluids, J. Non-Newton. Fluid Mech. 20 (1986) 143–171.

[19] J. van der Zanden, M. Hulsen, Mathematical and physical requirements for successful computations with viscoelastic fluid models, J. Non-Newton. Fluid Mech. 29 (1988) 93–117.

[20] M.A. Hulsen, Some properties and analytical expressions for plane flow of Leonov and Giesekus models, J. Non-Newton. Fluid Mech. 30 (1988) 85–92.

[21] M.A. Hulsen, A sufficient condition for a positive definite configuration tensor in differential models, J. Non-Newton. Fluid Mech. 38 (1990) 93–100.

[22] M. Aboubacar, H. Matallah, M.F. Webster, Highly elastic solutions for Oldroyd-B and Phan–Thien/Tanner fluids with a finite volume/element method: planar contraction flows, J. Non-Newton. Fluid Mech. 103 (2002) 65–103.

[23] M. Aboubacar, H. Matallah, H.R. Tamaddon-Jahromi, M.F. Webster, Numerical prediction of extensional flows in contraction geometries: hybrid finite volume/element method, J. Non-Newton. Fluid Mech. 104 (2002) 125–164.

[24] D.M. Binding, P.M. Phillips, T.N. Phillips, Contraction/expansion flows: the pressure drop and related issues, J. Non-Newton. Fluid Mech. 137 (2006) 31–38.

[25] J.P. Aguayo, H.R. Tamaddon-Jahromi, M.F. Webster, Excess pressure-drop estimation in contraction and expansion flows for constant shear-viscosity, extension strain-hardening fluids, J. Non-Newton. Fluid Mech. 153 (2008) 157–176.

[26] N.P. Thien, R.I. Tanner, A new constitutive equation derived from network theory, J. Non-Newton. Fluid Mech. 2 (1977) 353–365.

[27] H. Matallah, P. Townsend, M.F. Webster, Recovery and stress-splitting schemes for viscoelastic flows, J. Non-Newton. Fluid Mech. 75 (1998) 139–166.

[28] F. Belblidia, H. Matallah, M.F. Webster, Alternative subcell discretisations for viscoelastic flow: velocity-gradient approximation, J. Non-Newt. Fluid Mech. 151 (2008) 69–88.

[29] M.F. Webster, H.R. Tamaddon-Jahromi, M. Aboubacar, Time-dependent algorithms for viscoelastic flow: finite element/volume schemes, Numer. Meth. Part. Differ. Eq. 21 (2005) 272–296.

[30] P. Wapperom, M.F. Webster, A second-order hybrid finite-element/volume method for viscoelastic flows, J. Non-Newton. Fluid Mech. 79 (1998) 405–431.

[31] D.M. Hawken, P. Townsend, M.F. Webster, A comparison of gradient recovery methods in finite element calculations, Comm. Appl. Num. Meth. 7 (1991) 195–204.

[32] R.B. Bird, W.E. Stewart, E.N. Lightfoot, Transport Phenomena, John Wiley & Sons, New York, 1960.